MIT Libraries | DSpace@MIT

MIT Open Access Articles

Unsteady forces on spheres during free-surface water entry

The MIT Faculty has made this article openly available. ***Please share*** how this access benefits you. Your story matters.

Citation: Truscott, Tadd T., Brenden P. Epps, and Alexandra H. Techet. Unsteady Forces on Spheres During Free-surface Water Entry. Journal of Fluid Mechanics 704 (August 2, 2012): 173-210. © Cambridge University Press 2012

As Published: http://dx.doi.org/10.1017/jfm.2012.232

Publisher: Cambridge University Press

Persistent URL: http://hdl.handle.net/1721.1/80816

Version: Final published version: final published article, as it appeared in a journal, conference proceedings, or other formally published context

Terms of Use: Article is made available in accordance with the publisher's policy and may be subject to US copyright law. Please refer to the publisher's site for terms of use.

Massachusetts Institute of Technology

J. Fluid Mech. (2012), *vol.* 704, *pp.* 173–210. © Cambridge University Press 2012
doi:10.1017/jfm.2012.232

Unsteady forces on spheres during free-surface water entry

Tadd T. Truscott[1]†, Brenden P. Epps[2] and Alexandra H. Techet[2]

[1] Brigham Young University, Provo, UT 84604, USA

[2] Massachusetts Institute of Technology, Cambridge, MA 02139, USA

(Received 21 April 2011; revised 11 April 2012; accepted 14 May 2012;
first published online 2 July 2012)

We present a study of the forces during free-surface water entry of spheres of varying masses, diameters, and surface treatments. Previous studies have shown that the formation of a subsurface air cavity by a falling sphere is conditional upon impact speed and surface treatment. This study focuses on the forces experienced by the sphere in both cavity-forming and non-cavity-forming cases. Unsteady force estimates require accurate determination of the deceleration for both high and low mass ratios, especially as inertial and hydrodynamic effects approach equality. Using high-speed imaging, high-speed particle image velocimetry, and numerical simulation, we examine the nature of the forces in each case. The effect of mass ratio is shown, where a lighter sphere undergoes larger decelerations and more dramatic trajectory changes. In the non-cavity-forming cases, the forces are modulated by the growth and shedding of a strong, ring-like vortex structure. In the cavity-forming cases, little vorticity is shed by the sphere, and the forces are modulated by the unsteady pressure required for the opening and closing of the air cavity. A data-driven boundary-element-type method is developed to accurately describe the unsteady forces using cavity shape data from experiments.

Key words: computational methods, free surface, vortex shedding

1. Introduction

The impact of a solid sphere with a free surface of water can create an air cavity depending on the initial conditions and surface treatment. The forces acting on the sphere after impact are dictated by the cavity dynamics, or lack thereof, and the relative magnitude of the inertial force compared to the unsteady hydrodynamic forces. Experimental measurement of these forces has proven difficult for distances greater than one-half diameter beneath the surface because direct measurement via a force gauge is not feasible, and indirect measurement from position data requires highly accurate imaging and data processing techniques.

The complexity of the water entry problem has provided many opportunities for independent study. Phenomena studied in some detail include the initially small but fast jet that is ejected out below the sphere at the moment of impact with the free surface (Thoroddsen *et al.* 2004), the cavity ripples associated with the portion of the cavity that descends with the sphere after deep seal (cavity pinch-off) (Grumstrup,

† Email address for correspondence: truscott@byu.edu

Keller & Belmonte 2007), and the altered cavity shape and lift forces due to the addition of spin (Truscott & Techet 2009*a*,*b*). The hydrodynamic observations and measurements obtained from all of these studies can be applied to various naval hydrodynamics problems, such as the water entry of mines and the underwater launching of torpedoes. Industrial applications include structural interactions with the free surface such as ship slamming, extreme waves and weather on oil platforms, sprayed adhesives, and ink-jet printing. Even the sporting industry is interested in improving the water entry of various events, such as the water entry of swimmers and divers, reducing the drag of swimmers near the free surface, and the entry and exit of oars in rowing.

The majority of scientific investigations into water entry by spheres have focused on relatively heavy steel spheres, which have a mass ratio $m^* = \rho_s/\rho \approx 8$, where ρ_s is the density of the sphere and ρ is the density of water. As we will discuss herein, this means that their inertial force components tend to be very large, making it difficult to decipher the subtle unsteady hydrodynamics that occur after impact. Even the earliest studies used steel spheres, such as the hydrophobic steel spheres imaged by Worthington (1908) over a century ago. These images showed the classical air-cavity and splash patterns replicated in figure 1. Later, studies of water entry were used to design float planes impacting on the water surface (von Kármán 1929), torpedo water entry (May & Hoover 1963), and to examine general impact characteristics (Wagner 1932) (many more water-entry studies are reviewed by Korobkin & Pukhnachov 1988). More recent investigations by Duez *et al.* (2007) determined parameters necessary for cavity formation depending on kinematic, geometric and surface properties of the sphere. The effect of wettability on impact is addressed both numerically by Do-Quang & Amberg (2009) and experimentally by Duez *et al.* (2007) and Techet & Truscott (2011). Full characterizations of the sphere cavity dynamics are presented in Duclaux *et al.* (2007), for low Bond numbers in Aristoff & Bush (2009), and numerical estimates of cavity formation in Yan *et al.* (2009).

Typically, the studies that focus on the dynamics of water entry have chosen to vary only one parameter, such as the impact speed (May & Hoover 1963), atmospheric pressure (Gilbarg & Anderson 1948), impact angle (Asfar & Moore 1987) or surface treatment (Duez *et al.* 2007), while keeping all other parameters constant; and many studies have focused on the growth of the cavity and the pinch-off location for both spheres (Birkhoff & Isaacs 1951; Glasheen & McMahon 1996; Lee, Longoria & Wilson 1997; Aristoff *et al.* 2010) and disks (Gaudet 1998; Bergmann *et al.* 2009). Studies that have directly measured forces of impact have been limited to one-half diameter below the free surface due to experimental practicalities (Moghisi & Squire 1981). Goldman & Umbanhowar (2008) studied spheres impacting a granular medium and measured accelerations directly using accelerometers glued to the sphere. However, these accelerometers were hard wired to their data acquisition system, making this experimental setup impractical for the free-fall water-entry study considered herein. Forces below one-half diameter can be inferred from video analysis; however, it is highly sensitive to the imaging frame rate and processing procedures. Until recently, the imaging systems used were often relatively low speed (O(30 f.p.s.)) or the data processing was done in an overly simplistic fashion (e.g. fitting a simple quadratic curve to position data, thus implying a constant deceleration) or both.

Constant-deceleration models are sufficient for high-mass-ratio spheres, such as steel, since unsteady hydrodynamic forces are small compared to the inertial forces, and allow scientists to adequately explain the shape and evolution of the air cavity and subsequent pinch-off. However, this assumption does not allow accurate determination

FIGURE 1. Three spheres dropped from the same height ($h = 60$ cm), with the same diameter ($D = 2.54$ cm), impact speed ($U_0 = 3.43$ m s^{-1}), and Froude number ($Fr = U_0/\sqrt{gD} = 6.87$), coated with the same surface treatment to be hydrophobic (note: each sphere takes on a different static wetting angle $\theta > 90°$ due to the nature of the material as indicated for each sequence). The three cases have different mass ratios, $m^* = \rho_s/\rho$, as indicated. The time between images is 7.1 ms for all cases, and the time to deep seal (cavity pinch-off) is $t_{ds} = 70.3$, 73.1 and 72.9 ms for the acrylic, ceramic, and steel cases, respectively.

of the unsteady hydrodynamic forces acting on the sphere, especially for lower density spheres where the deceleration is no longer constant. We present results that detail the unsteady hydrodynamic forces acting on the sphere during descent and show that it is not sufficient to model the sphere position as a simple quadratic equation. Using high-speed imaging and advanced data processing techniques, we accurately measure the components of force acting on spheres of varying surface treatments and densities.

To illustrate our findings we present seven distinct cases (figures 1–3). Table 1 gives the details of these particular cases. The spheres studied are either treated with a surface coating that makes them hydrophobic or cleaned such that their surfaces are hydrophilic. Hydrophobicity is determined by the static contact angle, such that

$\theta > 90°$ hydrophobic, cavity-forming cases (figures 1 and 2)

$\theta < 90°$ hydrophilic, non-cavity-forming cases (figure 3).

It is clear from these figures that wetting angle affects cavity formation for a constant impact speed and mass ratio, but the forces acting on the sphere from cavity formation, or lack thereof, cannot be clearly identified from merely visual inspection.

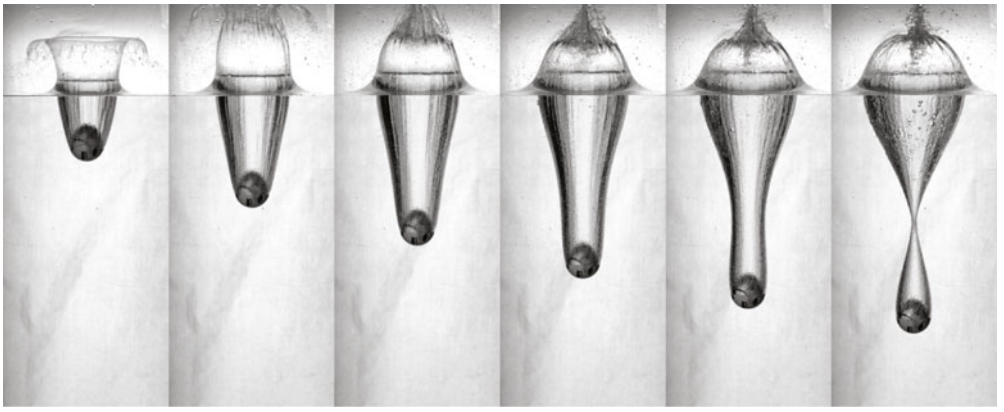

FIGURE 2. Film strip depicting water entry for the phenolic resin billiard ball case (see table 1: phenolic, $m^* = 1.8$, $D = 57.15$ mm, $U_0 = 5.67$ m s^{-1}, hydrophobic $\theta = 120°$). Images and simulations are synchronized in time, beginning at 16 ms after impact with 16.5 ms between each image. Time to deep seal is 98 ms.

The images also show that mass ratio has a significant effect on the cavity size for the hydrophobic spheres and on the trajectory and descent rate for both the hydrophobic and hydrophilic cases. We examine the variations and discuss regimes where these changes cause significant alterations to the forces.

This study was accomplished with the use of a high-speed digital method of gathering and analysing data. The results give a better estimation of the forces resulting in force coefficients that vary in time. In the cavity-forming cases, the unsteadiness is based upon the expanding and contracting cavity, which alters the pressure field around the sphere. In the non-cavity-forming cases, the unsteadiness is caused by the growth and shedding of ring-like vortical structures. Through the use of high-speed imaging, high-speed particle image velocimetry (PIV), and numerical simulation, the source and magnitude of the forcing are elucidated. The experimental methods used herein could be applied to future studies of objects in motion to gather force data.

2. Experimental methods

In order to determine the forces acting on the spheres after water entry, high-speed imaging captured the sphere descent and cavity formation for a range of mass ratios and impact velocities for both hydrophobic and hydrophilic spheres.

Impact speed was controlled by dropping the spheres from varying, discrete heights above the free surface. The acrylic tank used for high-speed imaging was 91.4 cm $\times$ 152.4 cm $\times$ 152.4 cm and held approximately 2200 L of water, and the glass tank used for PIV was 30 cm $\times$ 50 cm $\times$ 60 cm. The spheres were dropped using the same release mechanism as in Techet & Truscott (2011). A high-speed camera (IDT XS-3 CCD) was used to record each of the falling spheres. Figures 1 and 3 were recorded at 840 frames s^{-1} (f.p.s.) with a resolution of 756 $\times$ 1260 pixels. The field of view was 28.66 cm $\times$ 47.77 cm, yielding a 26.4 px cm^{-1} magnification. Figure 2 was recorded at 1000 f.p.s. with a resolution of 756 $\times$ 1260 pixels and 13.12 px cm^{-1} magnification. Data were recorded as the sphere descended, from just before impact until the sphere left the lower portion of the camera field of view.

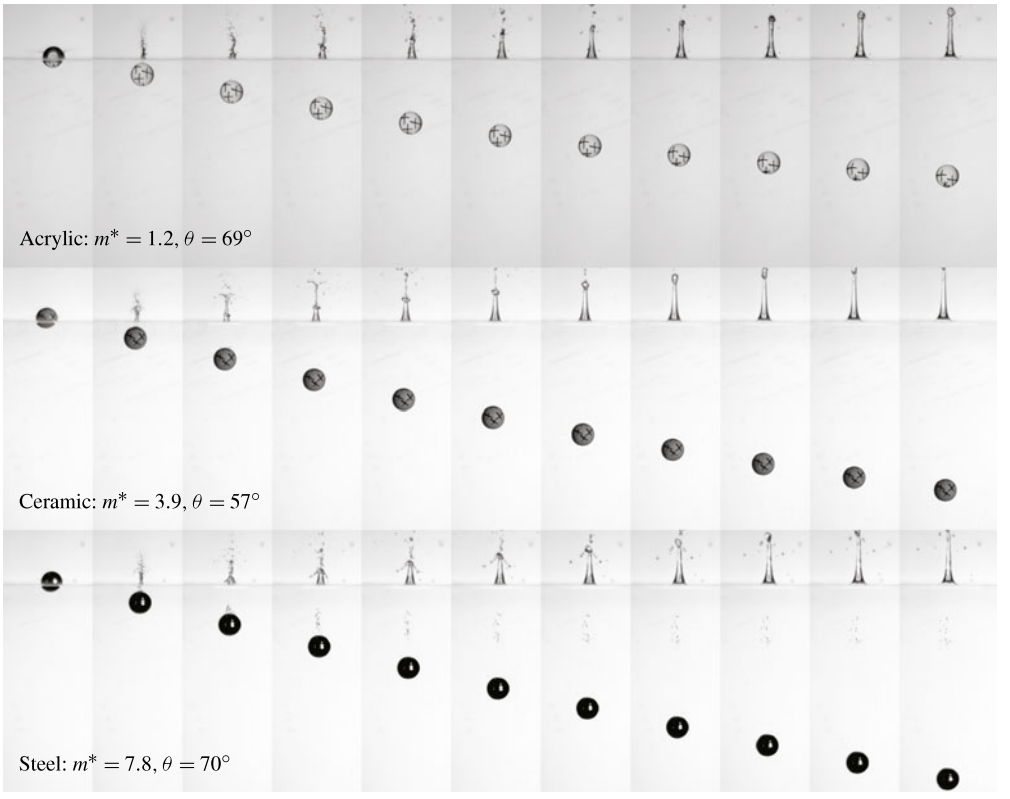

FIGURE 3. Three spheres dropped from the same height ($h = 60$ cm), with the same diameter ($D = 2.54$ cm), impact speed ($U_0 = 3.43$ m s^{-1}), and Froude number ($Fr = U_0/\sqrt{gD} = 6.87$), cleaned such that they are hydrophilic (static wetting angle $\theta < 90°$). No cavity is formed in these cases. The spheres have mass ratios corresponding to the spheres in figure 1. The time between images is 7.1 ms.

Material	Mass ratio	Diameter (mm)	Contact angle (deg.)/ roughness r.m.s. (μm)	Impact speed (m s^{-1})	t_{ds} (ms)
Acrylic	1.2	25.4	69°/0.29, 100°/2.73	3.43	70.3
Phenolic (billiard)	1.8	57.15	79°/0.80, 122°/1.95	5.67	98.0
Ceramic	3.9	25.4	57°/0.11, 118°/2.42	3.43	73.1
Steel	7.8	25.4	70°/0.01, 122°/2.40	3.43	72.9

TABLE 1. Spheres used in the present study. Advancing contact angles are given with error in the measurement of ±10° for hydrophilic ($\theta < 90°$) and hydrophobic ($\theta > 90°$) contact angles respectively. r.m.s. roughness measurements are given with error in the measurement of ±0.01 μm.

Image lighting was accomplished with backlighting by a bank of fluorescent lights to increase contrast, and several halogen spotlights in front of the tank to illuminate the foreground (figure 4).

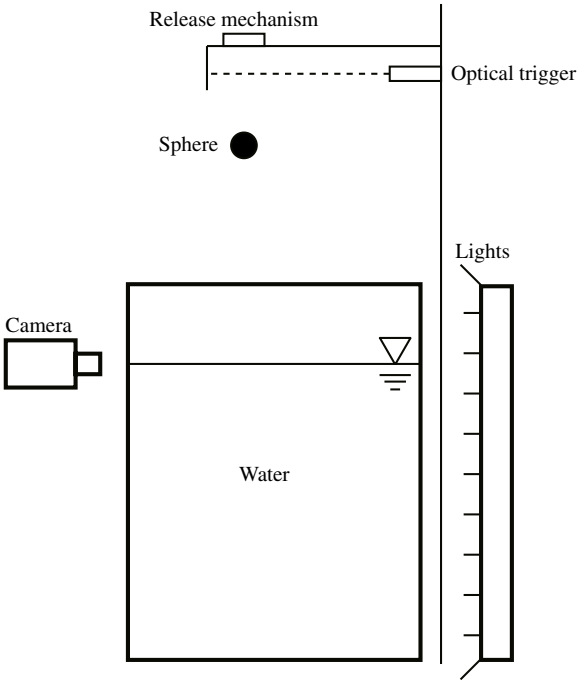

FIGURE 4. The acrylic impact tank was backlit with an array of fluorescent lights and frontlit by bright halogen spotlights so that the sphere could be imaged by the high-speed camera from one side. The spheres were dropped from discrete heights above the free surface.

The physical characteristics and parameters of the spheres used in this study are presented in table 1. The results presented herein focus on the 25.4 mm acrylic, ceramic, and steel spheres, as well as the 57.15 mm phenolic resin spheres (i.e. billiard balls). In addition to the range of sphere densities and sizes, two distinct surface treatments were considered: hydrophobic and hydrophilic. Hydrophobicity was accomplished using a spray coating (WX2100^{TM}), which was applied evenly and allowed to dry thoroughly. The hydrophobic coating produces both a new wetting angle and an associated surface roughness, which varies from the natural roughness of the materials. Hydrophilicity was achieved by cleaning the spheres in a three-step process using acetone, alcohol, and then ethanol, as described in Truscott (2009). The cleaned spheres were kept in a dust-free container and used within 20 min. of cleaning to ensure a uniformly hydrophilic surface.

Static wetting angles θ were measured using the static sessile drop method applied to each sphere, taking into account the curvature of the sphere. Roughness was measured using a Tencor P-10 Surface Profilometer. The profilometer data determined each sphere's surface profile, which includes both the surface roughness and the sphere radius curvature. The sphere's curvature was subtracted from the raw data to yield the roughness measurement. The root mean square (r.m.s.) of each roughness measurement is reported in table 1. This technique was also used to determine the roughness of both the coated and uncoated spheres.

Sphere position data were acquired from the raw images using the following method. Since the digital images were the source of the position data, it was necessary to measure the position of the sphere with sub-pixel accuracy and to avoid 'pixel-locking'

(artificially chosen pixel centres when the true value is between two pixels causing sub-pixel disparity), which would result in large errors in the inferred accelerations and forces. We employed a cross-correlation algorithm to determine the sphere position with sub-pixel accuracy, in a manner similar to that performed in PIV processing (e.g. Raffel *et al.* 1998). A template image of the sphere was cross-correlated with each image in the time series. The lower 1/3 of the sphere was used as a template to find the position in each image. This ensures that the cavity does not interfere with the accuracy of the correlation technique. The correlation peak was fitted with a Gaussian curve to determine the peak location within approximately ± 0.025 pixels (9 μm), similar to the peak fitting implementation employed in particle imaging velocimetry processing algorithms (e.g. Raffel *et al.* 1998). Thus, the accuracy of the position data corresponds to $\pm 0.04\,\%$ of the diameter of the 25.4 cm spheres shown in figures 1 and 3.

The sphere position and cavity data were zeroed with the free surface, making the free surface the origin of both time and space such that the centre of the sphere was at the undisturbed free-surface elevation at $t = 0$, and any inclination of the free surface resulting from camera rotation was removed from the images. In the cavity-forming cases, the Canny edge-finding technique was used to determine the cavity shape by tracing the highly contrasted edges of the cavity as viewed in figure 1. These cavity data were used to seed the potential flow model introduced in § 3.3.

Sphere velocity and acceleration are (not quite as simply) the temporal derivatives of the measured position data. It is well known that taking derivatives of measured data via finite differences (i.e. $U(t) = \Delta z/\Delta t$) amplifies any measurement error that may be present in the data. Error amplification is avoided by inferring the required derivative from that of an analytic curve fitted to the data. Thus, finding the derivative of experimental data amounts to fitting the analytic curve that best approximates the true function that the data represents.

To determine the velocity and acceleration of the spheres, the position data were fitted with a quintic smoothing spline (de Boor 1978), where the smoothing parameter was chosen using the procedure developed by Epps, Truscott & Techet (2010). This procedure ensures that the spline roughness is minimized, thus ensuring a smooth curve, while simultaneously minimizing error to the measured position data. This provides the most accurate representation of the data possible, while filtering out the measurement error. The velocity and acceleration of the sphere are then determined analytically from the fitted spline.

Epps *et al.* (2010) show good agreement between instantaneous velocities and accelerations predicted by the smoothing spline and those estimated using local least-squares regression (Cleveland 1979). Validation of the spline fitting procedure comes from the fact that the spline derivatives are relatively smooth compared to the least-square derivatives and is discussed further in the context of the results in § 3.3.

Both the cavity-forming and non-cavity-forming cases were also investigated using high-speed PIV to gather information about the corresponding flow fields. The setup was similar to that used for the standard high-speed imaging, but instead of using backlighting, a laser sheet illuminated a plane along the vertical mid-line axis of the falling sphere. The tank was seeded with 50 μm polyamide neutrally buoyant particles that were illuminated by the 2.2 W laser (LaVision) at 532 nm; the laser was fitted with an optical lens that produced a 20° fan of light. The IDT XS-3 camera was used to image the particles in the laser sheet with a resolution of 404×1280 pixels and a field of view of 8.14 cm × 25.80 cm, yielding 49.61 px cm^{-1} magnification at 2020 f.p.s. PIV data were collected and processed using the LaVision DaVis

7.2 software package. A multipass, cross-correlation processing algorithm with a final interrogation window size of 16×16 pixels and 50 % overlap was used for processing all of the images. The output was a velocity field with 160×50 vectors.

The velocity field data were further processed using the procedure described in Epps & Techet (2007) to determine the circulation and impulse of the vortices shed from the sphere. Circulation was computed at each time step using Stokes' theorem

$$\Gamma = \sum_{ij} \omega_{ij}\, \delta A \tag{2.1}$$

where ω_{ij} is the vorticity at a point (i, j), and $\delta A = (8\ \text{px})^2 = 0.163\ \text{cm}^2$ is the area of each PIV interrogation window. The area over which the summation occurs is bounded by an isovorticity contour (Gharib, Rambod & Shariff 1998), where herein we chose the isovorticity level equivalent to 25 % of the maximum circulation for each vortex. The measurement error for the circulation (2.1) is less than 15 %, which can be seen in the scatter in the impulse data shown in figure 12(*b*). This is consistent with Epps & Techet (2007), who report 14 % uncertainty in their circulation measurement. Further, the uncertainty in (2.1) can be examined by comparing the positive and negative vortex patches seen in figures 11 or 13, which represent slices through two opposite halves of the vortex ring. The magnitude of circulation of these patches is observed to be equal to within 20 %, which follows classical laws for conservation of circulation around a vortex ring.

3. Experimental results

Herein we consider the results of seven cases: the four hydrophobic cases from figures 1 and 2, the three hydrophilic cases from figure 3. These representative cases span a wide range of mass ratios, two surface coatings, and two different diameters (table 1).

Figure 1 depicts the evolution of the cavity formation during water entry for three hydrophobic spheres, each with different mass ratios but the same hydrophobic coating and impact speed. It is apparent that the heaviest spheres descend fastest. The hydrophobic acrylic sphere decelerates more rapidly and reaches pinch-off at a much shallower depth, but a similar time, compared to the hydrophobic ceramic and steel spheres. While the depth at which deep seal occurs is known to be an increasing function of mass ratio, the non-dimensional time to deep seal ($\tau = t_{ds}\,(2g/D)^{0.5}$) remains constant (Truscott & Techet 2009*b*). For the cases presented here, deep seal occurs at a non-dimensional time of $\tau = 1.78 \pm 0.0752$, which is slightly larger than those reported by Gilbarg & Anderson (1948) ($\tau = 1.74$) and Truscott & Techet (2009*b*) ($\tau = 1.726 \pm 0.0688$), but is within the error bounds of their measurements. Further analytical treatment of cavity features for decelerating sphere impact is discussed in Aristoff *et al.* (2010).

As a hydrophilic sphere passes through the free surface, the water it displaces comes back together at the top of the sphere, creating a jet that ascends above the free surface, but no subsurface air cavity, as shown in figure 3. This phenomenon was first witnessed by Worthington (1908) when clean glass spheres were dropped in water, and is theoretically explained for smooth spheres by Duez *et al.* (2007). Once the sphere is underwater, the backlit video images do not reveal much about the flow field. However, they can be used to inspect the trajectory of the spheres in time and infer forces from position data, as discussed in the following section.

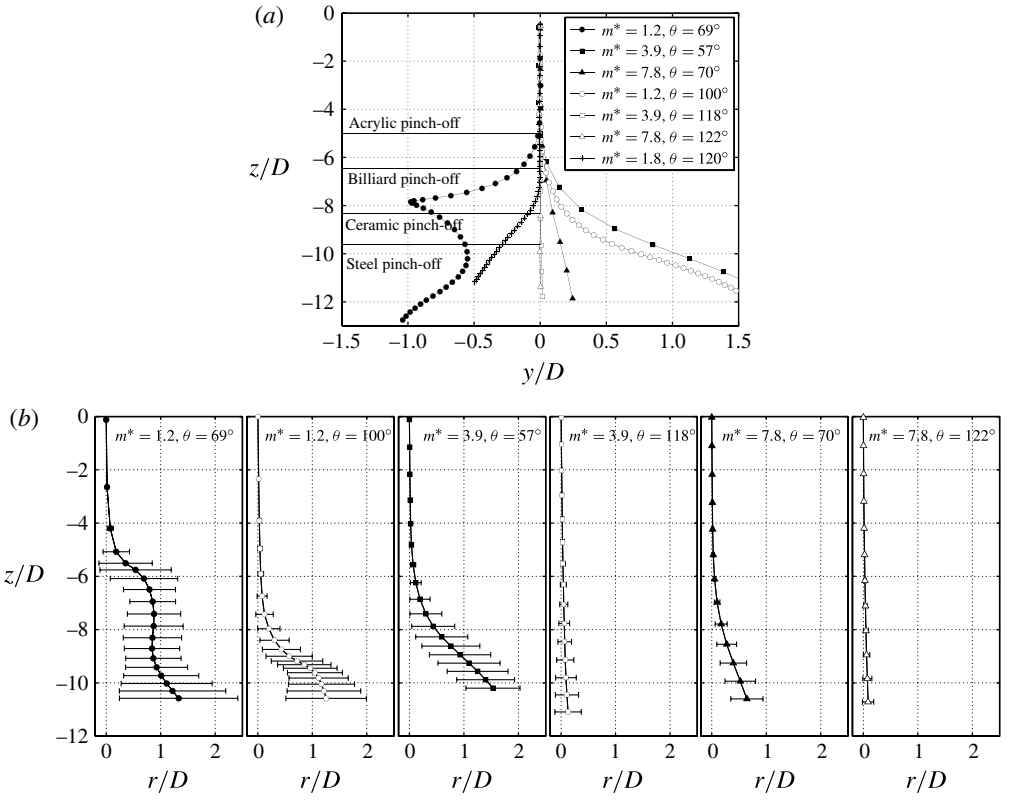

FIGURE 5. (*a*) Lateral y and vertical z position of the spheres for the four hydrophobic cases presented in figures 1 and 2 (open symbols) and the three hydrophilic cases shown in figure 3 (filled symbols). Position is normalized by sphere diameter and every tenth data point is plotted. The location of the sphere at pinch-off is noted by a horizontal line for each hydrophobic case. Position measurement error is $\pm 0.04\,\%D$, approximately the thickness of the lines as shown. (*b*) Repeatability: mean trajectory based on the radial deviation from vertical (averaged over 10 trials); the error bars represent the 95 % confidence interval.

3.1. *Trajectory, velocity, and acceleration*

The y–z trajectory of each sphere is presented in figure 5(*a*), showing the path of the seven cases presented in figures 1–3. Initially all of the spheres descend vertically until about $z/D \approx -5$, where several cases deviate laterally. All of the hydrophobic cases have the same time to deep seal, as expected, but are located at different depths when deep seal occurs. Deep seal is marked in figure 5(*a*) by a horizontal line for each hydrophobic case.

After pinch-off, the hydrophobic acrylic sphere curves off to the side. The hydrophobic steel and ceramic spheres continue on their vertical descent moments after pinch-off, until they leave the camera field of view. From observations not presented herein, the steel and ceramic spheres do eventually deviate from their vertical trajectories, but this was not captured in our field of view. This deviation is likely to be due to vortex shedding and is illustrated using PIV for the non-cavity-forming cases in § 4.1. The cavities produced by the hydrophobic spheres prevent

vortex shedding in the wake until the moment of deep seal, at which point vortex shedding can then occur.

In general, all of the hydrophilic spheres have some deviation from vertical descent. The acrylic and ceramic spheres experience the greatest lateral translation, while the steel spheres ($m^* = 7.8$) display much more subtle horizontal displacement. The acrylic sphere ($m^* = 1.2, \theta = 69°$) almost comes to a complete stop in the z-direction as it descends; the kink in its trajectory indicates the position where the sphere changed direction. This sudden change is due to asymmetrical vortex shedding around the sphere, and is similar to results shown in Horowitz & Williamson (2008)'s detailed study of rising and falling spheres with mass ratios from 0.08 to 1.41. In their study, Horowitz & Williamson (2008) concluded that descending spheres with a mass ratio <1.41 or rising spheres with a mass ratio >0.41 would follow an oblique rectilinear path, meaning that they would tend to travel vertically with somewhat constant horizontal displacement in y. However, spheres with mass ratios <0.11 would always vibrate in a single vertical plane. Here we find that spheres with mass ratios >1.4 have oblique rectilinear paths, and spheres with mass ratios near 1.2 seem to vibrate as they descend, similar to those below 0.11 in Horowitz & Williamson (2008). Further evidence of this vortex-induced oscillation is presented in the PIV results in § 4.1.

The variation in lateral deviation from run to run was investigated by synchronizing two cameras to measure x and y positions and combining these data to form a radial deviation from the vertical. Figure 5(b) shows the mean trajectory averaged over 10 trials of each 25.4 mm sphere type; the 95 % confidence intervals shown were computed using a student's t-distribution. These results indicate that the experiment is very repeatable for early times (i.e. shallower depths), before cavity collapse or vortex shedding occurs. The trajectory of the sphere after vortex shedding depends on the direction of the shed vortex, which is random, and hence results in larger confidence intervals. Nevertheless, the results in figure 5(a) are representative cases.

Vertical descent velocity $\mathrm{d}z/\mathrm{d}t$ (figure 6), as a function of time, is calculated from the z-position data using the spline method discussed in § 2. Data are plotted versus non-dimensionalized time t/t_{ds}, where t_{ds} is the time to deep seal for each mass ratio. Velocity is shown beginning with the first frame after the sphere is submerged one full radius below the free surface. At this point the acrylic sphere has already decelerated to almost 85 % of its initial velocity, whereas the larger-mass-ratio spheres are still travelling near the impact speed, U_0. In the case of the heavier spheres, inertial effects dominate and hydrodynamic forces have not yet had a significant impact on the sphere velocity. Conversely, the rapid deceleration of the acrylic sphere can be attributed to the greater relative influence of the hydrodynamic forces compared to the inertial forces. The rate of change of velocity appears to be relatively constant for all three hydrophobic cases at early time steps before pinch-off. At pinch-off the rate of change in the velocity begins to decrease, most visibly for the acrylic sphere.

The terminal velocity U_t/U_0 of each sphere is shown in figure 6 for reference. Terminal velocity is determined theoretically by balancing weight ($(4/3)\pi R^3 \rho_s g$) with buoyancy ($(4/3)\pi R^3 \rho g$) and steady-state drag ($(1/2)\rho U_t^2 C_d \pi R^2$), which yields

$$U_t = \sqrt{\frac{8}{3}\frac{gR}{C_d}(m^* - 1)}, \tag{3.1}$$

where R is the sphere radius. Here, we assume a steady-state drag coefficient of $C_d = 0.5$, which is typical for the Reynolds numbers of these experiments ($Re_t =$

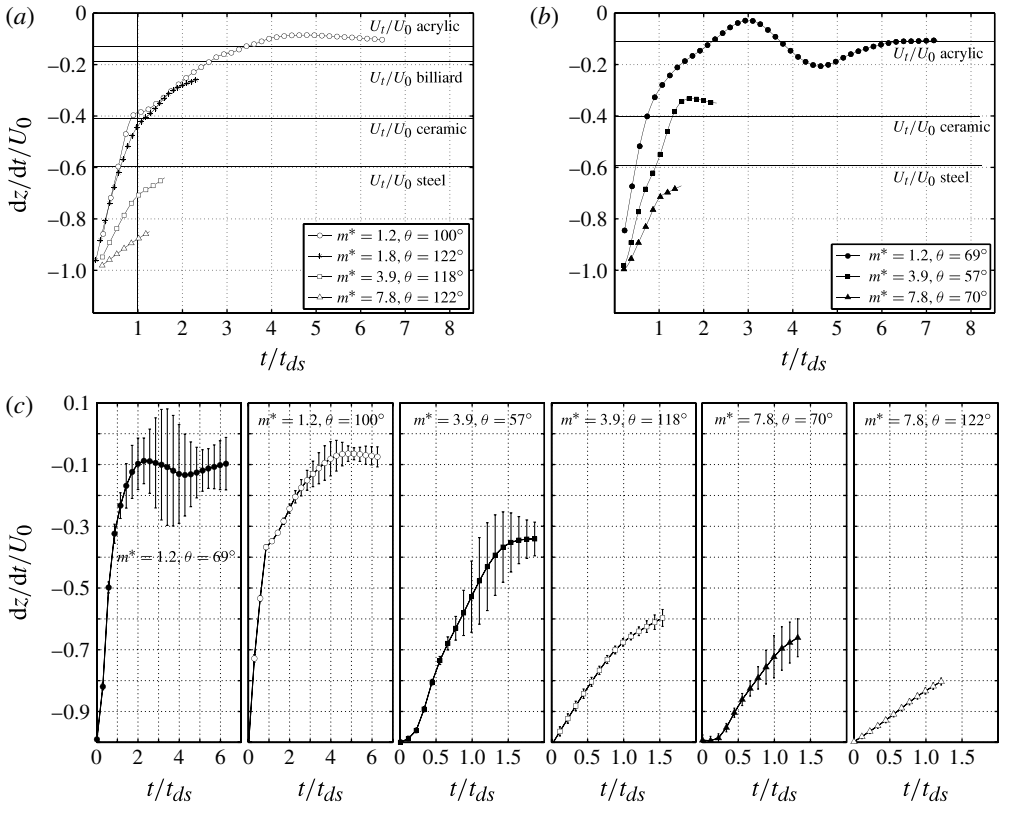

FIGURE 6. Time trace of the vertical velocity $\mathrm{d}z/\mathrm{d}t$ of the hydrophobic (cavity-forming) (*a*) and hydrophilic (non-cavity-forming) (*b*) cases derived from figure 5(*a*). Velocity is normalized by impact speed U_0 and plotted versus non-dimensionalized time t/t_{ds}, where t_{ds} is the time to deep seal for each mass ratio (table 1). Terminal velocity is normalized by impact speed U_t/U_0 for each mass ratio and shown for reference. Since the acrylic spheres decelerate rapidly, they reach terminal velocity while still in the camera field of view, whereas the ceramic and steel spheres are out of view just after pinch-off. Every tenth time step is plotted. (*c*) Repeatability: mean velocity (averaged over 10 trials) and 95 % confidence interval.

$U_tD/\nu \sim 10^4$). Terminal velocity of the four materials by increasing density are: -0.36, -0.19, -1.39 and -2.13. Note that the acrylic sphere approaches terminal velocity for long times ($t \gg t_{ds}$) and exhibits underdamped behaviour. The ceramic and steel spheres exit the field of view before terminal velocity is reached for the hydrophobic cases, but the hydrophilic ceramic sphere nears terminal velocity within the field of view. The repeatability of the velocity measurements is presented in figure 6(*c*). The hydrophobic cases are very consistent trial to trial (i.e. small confidence intervals) for early times (before cavity pinch-off), and likewise, the hydrophilic cases are quite repeatable for early times (before vortex shedding).

The acceleration of the spheres can be considered by taking the second derivative of the spline fitted to the $z(t)$ position data. Accelerations, normalized by t_{ds}/U_0, are plotted in figure 7; positive values indicate deceleration. The hydrophobic cases show a relatively constant deceleration for early times, and then rapid changes in acceleration

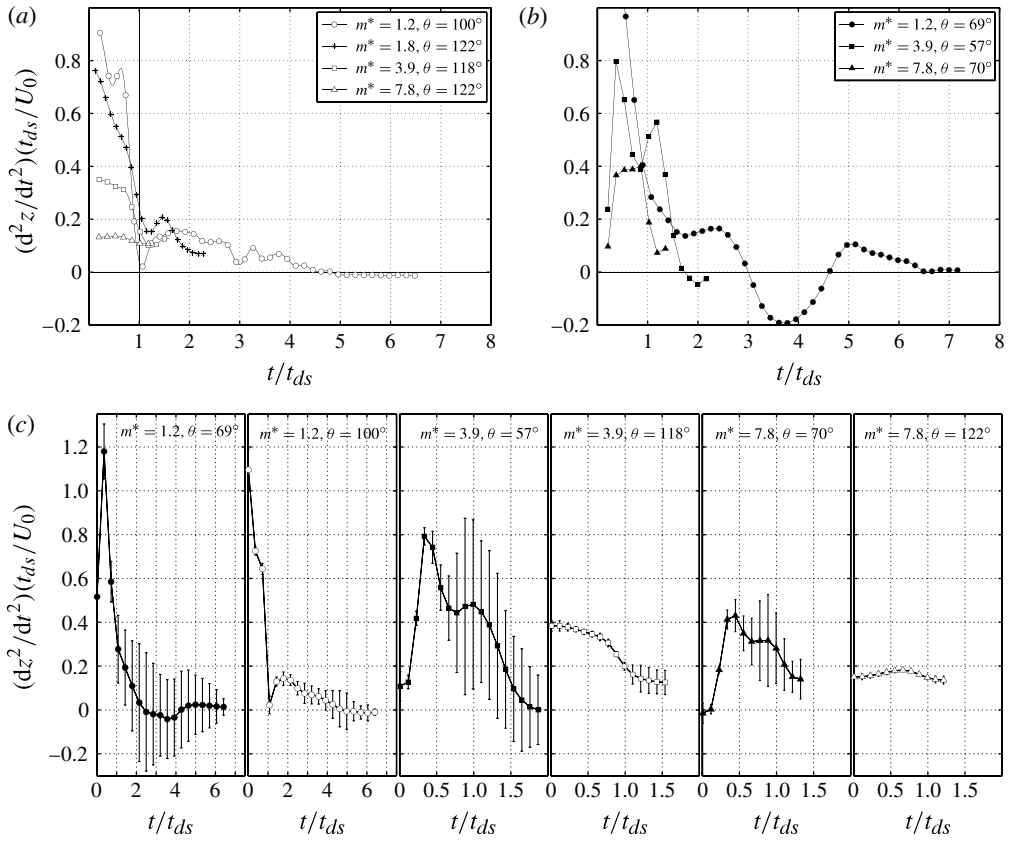

FIGURE 7. Acceleration of the spheres presented in figure 1–figure 3, plotted versus time non-dimensionalized by the time to deep seal for each mass ratio (table 1): (*a*) hydrophobic (cavity-forming); (*b*) hydrophilic (non-cavity-forming). Every tenth time step is plotted. (*c*) Repeatability: mean acceleration (averaged over 10 trials) and 95 % confidence interval.

during cavity pinch-off. In particular, figure 7(*a*) shows a tremendous drop in the acceleration of the spheres just before the cavity pinch-off event; clearly not a simple linear deceleration as would be predicted by a third-order quadratic fit to the position data. As will be discussed in § 5, this is due to the unsteady forces acting on the sphere due to cavity closure.

Remarkably, the maximum decelerations are higher for all three hydrophilic cases. This indicates a higher resistive force compared to the cavity-forming, hydrophobic cases, which is somewhat surprising. In the sections that follow, we show that these large forces in the hydrophilic cases are due to unsteady vortex shedding, whereas in the hydrophobic cases, vortex shedding is suppressed, and thus the forces are lower. Repeatability of the acceleration measurements is presented in figure 7(*c*); these data show the same trend as the velocity data in figure 6(*c*), namely that the experimental results are very repeatable for early times.

3.2. *Forces*

The accelerations calculated in the previous section can be used to determine the total hydrodynamic force F acting on the sphere during the experiment. While one may

be tempted to assume a model for F at this time (e.g. the classical model of the sum of buoyancy, added mass, steady-state drag, etc.), there is no need to confine ourselves to such a model *a priori*. For now, we are simply concerned with using the experimental acceleration data to infer the total hydrodynamic force acting on the sphere. In subsequent sections, we will develop models that demonstrate the dominant components acting in each of the hydrophobic and hydrophilic cases.

The net upward force acting on the sphere (which produces an upward acceleration) is the sum of the total hydrodynamic force $F(t)$ and the weight of the sphere

$$m\ddot{z}(t) = F(t) - mg. \tag{3.2}$$

The hydrodynamic force on the sphere is, in general, the sum of pressure forces, viscous traction forces, and surface tension forces:

$$F(t) = \boldsymbol{F} \cdot \hat{\boldsymbol{k}} = \int_S p(-\hat{\boldsymbol{n}} \cdot \hat{\boldsymbol{k}})\, \mathrm{d}S + \int_S \hat{\boldsymbol{n}} \cdot \boldsymbol{T} \cdot \hat{\boldsymbol{k}}\, \mathrm{d}S + 2\pi R\sigma \cos\varphi, \tag{3.3}$$

where $\hat{\boldsymbol{k}}$ is the unit vector in the z-direction (positive upwards), $\hat{\boldsymbol{n}}$ is the unit normal vector directed out of the sphere, $\boldsymbol{T}$ is the viscous stress tensor, and φ is the angle the cavity makes with $\hat{\boldsymbol{k}}$ at the contact line (if a cavity exists). It is important to reiterate that F is the total hydrodynamic force and not a drag force in the traditional sense.

For the experiments considered herein, typical values of the relevant non-dimensional parameters are as follows: $\rho_s/\rho \sim O(1)$, $U^2/gD \sim O(1)$ and $Re \sim O(10^4)$. Under these conditions, the viscous skin friction force is small compared to the weight of the sphere: $(\rho U^2 R^2 Re^{-1/2})/\rho_s g R^3 \sim (\rho/\rho_s)(U^2/gD)Re^{-1/2} \sim 10^{-2}$. Similarly, the surface tension force is also small compared to the weight: $R\sigma\cos\varphi/\rho_s g R^3 \sim (\rho/\rho_s)(\sigma/\rho g R^2) \sim 10^{-3}$. Thus, if the net hydrodynamic force acting on the sphere is significant with respect to the weight of the sphere, then it is dominated by the pressure force, which includes the unsteady added mass and hydrostatic buoyancy forces. In the hydrophobic cases, the pressure force is modulated by the unsteady pressure required to create the subsurface air cavity. In the hydrophilic cases, no cavity is present, and the pressure force is modulated by the growth and shedding of vortical structures in the wake.

Regardless of the nature of the hydrodynamic force, the total hydrodynamic force can be inferred from the acceleration of the sphere using (3.2). The experimental velocity and acceleration data can be used to compute the total hydrodynamic force coefficient

$$C_F(t) \equiv \frac{F(t)}{\frac{1}{2}\rho\,[U(t)]^2\,\pi R^2} = \frac{m(\ddot{z}(t) + g)}{\frac{1}{2}\rho\,[U(t)]^2\,\pi R^2} \tag{3.4}$$

where $U \equiv -\dot{z}$ is the instantaneous speed of the sphere.

For reference, a *terminal force coefficient* may be calculated when the sphere has reached terminal velocity, where by definition, it is assumed that the hydrodynamic force is due only to buoyancy and steady-state drag. The terminal force coefficient is derived from (3.1) and (3.4) as

$$C_{F_t} = \frac{m^*}{m^* - 1} C_d. \tag{3.5}$$

The force coefficients for the seven cases are plotted in figure 8. Figures 8(*a*) and 8(*b*) compare the mass ratios for each surface treatment (hydrophobic and hydrophilic, respectively); figure 8(*c–e*) compares the forces for each surface treatment at the three

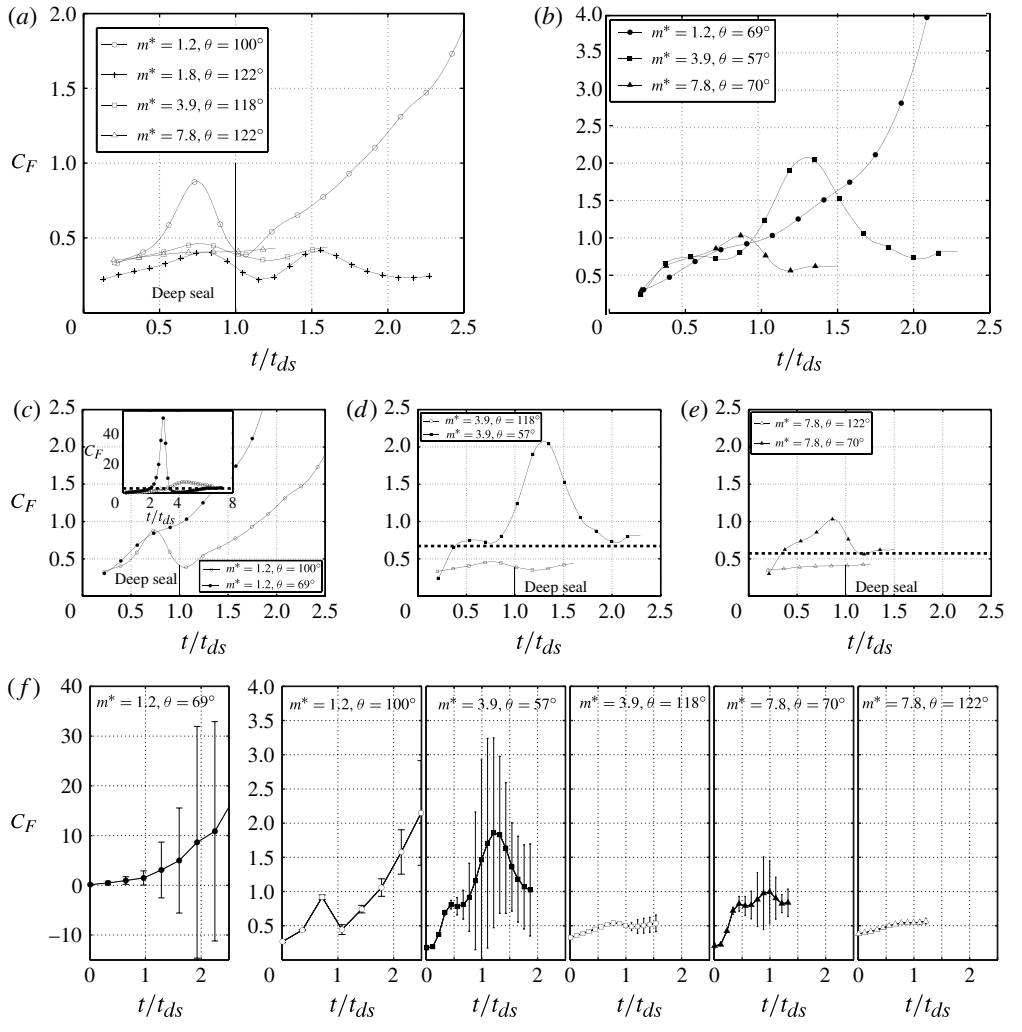

FIGURE 8. Force coefficients for the hydrophobic (*a*) and hydrophilic (*b*) spheres, plotted versus non-dimensional time. In (*c–e*) the hydrophobic and hydrophilic cases for each mass ratio (acrylic, ceramic and steel, respectively) are compared to directly highlight the differences between the two surface treatments. The inset in (*c*) shows the entire time sequence for the acrylic sphere, whereas the time-axis for (*c*) matches that of (*d,e*). Overall, the hydrophobic spheres tend to have lower force coefficients than the hydrophilic spheres. Horizontal lines (——) denote the terminal force coefficient (3.5). Solid lines include all force coefficient data points, and every tenth time step is plotted as a symbol for clarity. (*f*) Repeatability: mean force coefficient (averaged over 10 trials) and 95 % confidence interval.

specific mass ratios considered. Terminal force coefficients of the four materials by increasing density are: 3.07, 1.167, 0.67 and 0.57.

Comparing the hydrophobic and hydrophilic acrylic cases in figure 8(*c*), both C_F curves are similar up to $t/t_{ds} \approx 0.75$. The force coefficient for the hydrophobic sphere then falls before deep seal at $t/t_{ds} = 1$. In contrast, C_F for the hydrophilic sphere rises

steadily to a non-dimensional time $t/t_{ds} \approx 3$ (see figure 8*c* inset), at which point the sphere virtually stops moving in the z-direction. After this event, the force coefficient diminishes as quickly as it rose and reaches a minimum near $t/t_{ds} = 4.5$. The force coefficient for both the hydrophobic and hydrophilic cases approaches the terminal force coefficient for times $t/t_{ds} > 7$ (i.e. well after cavity collapse).

The ceramic cases shown in figure 8(*d*) exhibit similar behaviour. The hydrophilic (non-cavity-forming) ceramic sphere experiences larger force coefficients than its hydrophobic (cavity-forming) counterpart. The hydrophobic ceramic sphere has a maximum force coefficient before deep seal and a minimum after, similar to the acrylic case. These trends hold true for even larger mass ratios (e.g. the steel case shown in figure 8*e*), where the effect of the unsteady forcing becomes progressively less apparent and the inertial term ($m\ddot{z}$) dominates the signal. Repeatability (figure 8*f*) over 10 trials once again reveals that the experiment is very consistent for early times (before cavity collapse or vortex shedding).

In general, the data indicate that spheres without cavities tend to have higher force coefficients than their cavity-forming counterparts. In the following two sections, we will show that this difference is due to unsteady vortex formation, which is not present in the cavity-forming cases. Furthermore, the force coefficients are neither constant nor linear for any of the sphere entry cases, yet approach linearity for the larger masses (e.g. $m^* = 7.8$).

3.3. *On the estimation of forces from position data*

As described in detail in Epps *et al.* (2010), the velocity, acceleration, and force coefficients are derived from a smoothing spline fit to the measured position data. This regression is necessary to prevent amplification of the measurement error when taking the required derivatives, as happens when using simple finite differences. In order to smooth the data, the fitted spline $s(t)$ is allowed an 'error tolerance' $E = \sum_{i=1}^{N} |s(t_i) - z(t_i)|^2 \, \Delta t$, such that it can pass smoothly through the data. The amount of smoothing is characterized by the spline 'roughness', defined for the quintic spline as $R = \int |\mathrm{d}^3 s/\mathrm{d}t^3|^2 \, \mathrm{d}t$. Each of several candidate splines is shown in figure 9(*a*).

Figure 9 shows the effect that choosing alternative spline fits has on the position, velocity, acceleration, and instantaneous force coefficient for the billiard ball case (figure 2). Since the selected spline is reported in figures 5(*a*)–8, the choice of spline is, in a sense, the reliability of the measurement for a particular trial. Thus, figure 9 gives a sense of the 'error bars' for figures 5(*a*)–8. Inter-trial repeatability can be inferred by comparing the force coefficients from different trials presented in figures 12(*a*), 14(*a*) and 16(*b*).

The candidate position splines shown in figure 9(*b*) are indistinguishable, which indicates that the 'error bars' in the position data reported in figure 5(*a*) are smaller than the width of the curves shown in figure 9(*b*). A more quantitative estimate of the measurement error is as follows. If the measurement error is $O(\epsilon)$, then the spline error is approximately $E \approx N\epsilon^2 \Delta t$. For this case, $N = 230$, $\Delta t = 0.001$ s, and the selected spline has $E = 2.5 \times 10^{-9}$ m^2 s error, so $\epsilon \approx \sqrt{E/(N\Delta t)} \approx 0.1$ mm ≈ 0.13 px, which is equivalent to 0.2 % of the billiard ball diameter. The velocity curves in figure 9(*c*) also match well, except near pinch-off, indicating high precision in the velocity results reported in figure 6.

The acceleration and force coefficient curves in figure 9(*d*,*e*) show the largest sensitivity to a poor choice of a smoothing spline. The orange spline has allowed too large an error tolerance, so it does not track the data during cavity deep seal. Conversely, the red spine is constrained too tightly to the data, so it does not properly

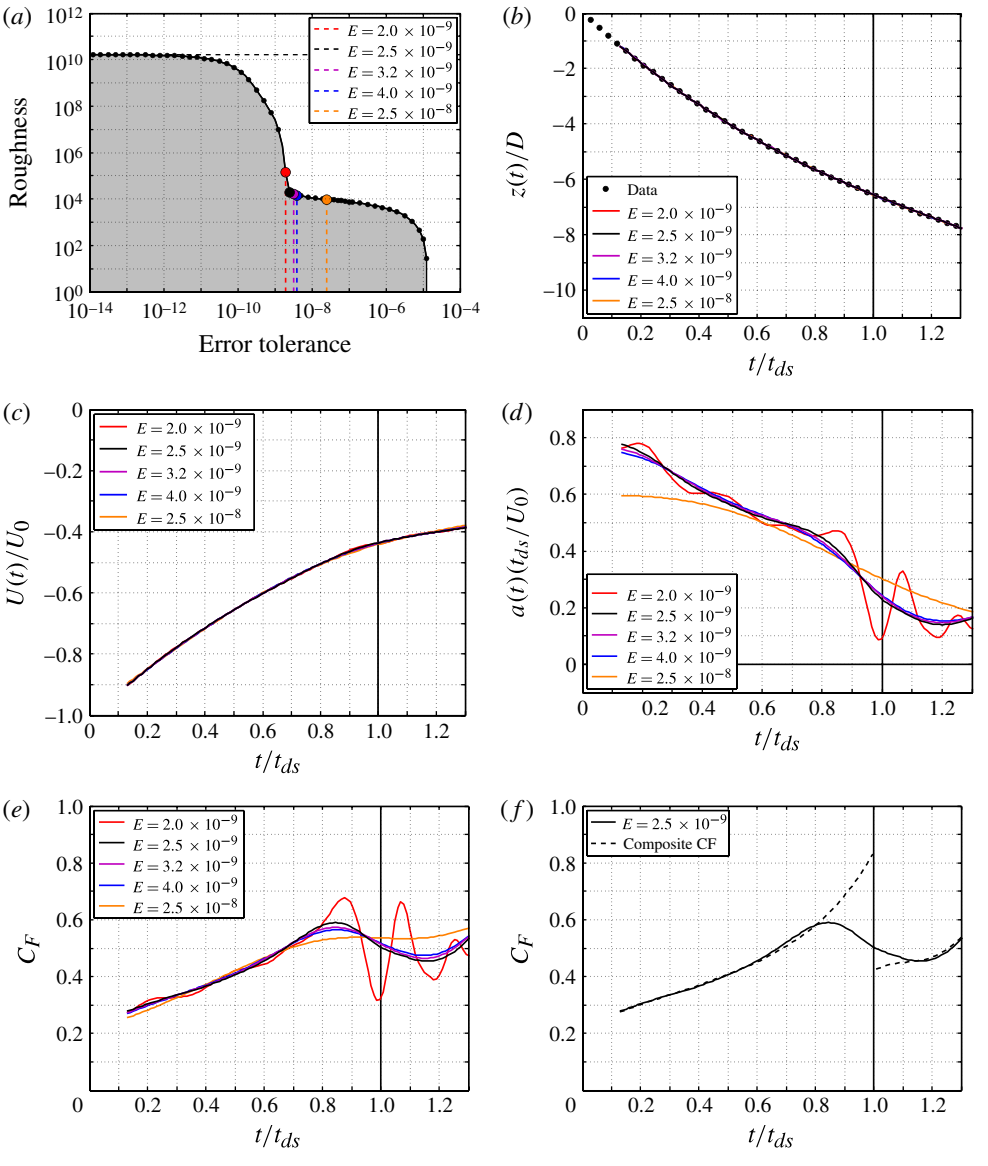

FIGURE 9. (*a*) Smoothing spline roughness versus error tolerance for candidate splines fit to the position data for the billiard ball case (figure 2). (*b*) Position data $z(t)$ and candidate splines $s(t)$, showing that the uncertainty in the fitting procedure (i.e. the error bar width) is less than the thickness of the line. Every fourth data point is shown. (*c*) Velocity $U(t) = \mathrm{d}s/\mathrm{d}t$ derived from candidate splines. (*d*) Acceleration $a(t) = \mathrm{d}^2s/\mathrm{d}t^2$ derived from candidate splines. (*e*) Force coefficient (3.4) derived from candidate splines. The '$E = 2.5 \times 10^{-9}$' spline offers the best trade-off between roughness and error and, thus, best represents the data. (f) Force coefficient derived from the best-fit spline ($E = 2.5 \times 10^{-9}$), as well as a 'composite force coefficient' derived by separately fitting splines to the data split before and after cavity deep seal.

smooth the measurement error. The blue, purple, and black splines all closely overlay, again indicating high precision in the results reported in figures 7 and 8. The black spline ($E = 2.5 \times 10^{-9}$) offers the best trade-off between roughness and error tolerance, as it most closely follows the data without incurring roughness due to measurement error, as discussed in Epps *et al.* (2010).

Comparing the force coefficients in figure 9(*e*), it is evident that as error tolerance is reduced, the force coefficient rises and falls more dramatically during pinch-off. Since the cavity closure event is quite rapid, it is anticipated that it causes a dramatic drop in the net force acting on the sphere at the moment of pinch-off. As a thought experiment, consider the effects of hydrostatic pressure alone. While the cavity exists, the hydrostatic pressure force acting upwards on the bottom of the sphere is unabated. However, in the moments after pinch-off, water rushes in above the sphere, and hydrostatic pressure builds above the sphere. This rapid pressure increase above the sphere reduces the net upwards hydrostatic pressure force quite rapidly after pinch-off. Thus, it is anticipated that the total force on the sphere should fall dramatically in the moments after pinch-off and that the instantaneous force coefficient may be nearly singular for rapid cavity closure cases such as that shown in figure 2.

To create an 'upper limit' for how singular the change in total force may be during pinch-off, consider a *composite force coefficient* formed by fitting two splines, one to the position data before pinch-off and the other to the position data after pinch-off, and then finding the force coefficients from each of these splines. Since each spline terminates at the pinch-off time, this composite spline is not required to be continuous through pinch-off. The composite force coefficient shown in figure 9(*f*) agrees well with the nominal force coefficient for times away from pinch-off, as expected from the nature of the spline fitting procedure. However, the composite force coefficient continues to rise until the time of pinch-off and then falls singularly, whereas the nominal force coefficient smooths the forces during pinch-off (since the single spline fit is required to be continuous through pinch-off). It is anticipated that the forces are not truly singular, so the actual force coefficient may resemble something between these predictions, or it may rise until pinch-off and then fall in a smooth manner in the few moments after pinch-off.

Figure 10 shows the nominal force coefficient and composite force coefficient for all four cases in figures 1 and 2, illustrating the effect of mass ratio. The high-mass-ratio steel sphere experiences nearly constant force coefficients during the impact event, whereas the low-mass-ratio acrylic sphere experiences highly unsteady force coefficients. We revisit this in § 5.3 where we present a potential model to unravel the nature of the unsteady forcing leading up to pinch-off (figure 19).

4. Force model: non-cavity-forming cases

4.1. *PIV of non-cavity-forming cases*

Using high-speed PIV, the unsteady flow field around the non-cavity-forming spheres is now characterized, and the vortical wake signature is correlated with the forces acting on these spheres. Since the hydrophilic acrylic spheres ($m^* = 1.2$) have the greatest decelerations and largest force coefficients, the acrylic sphere is presented first. Figure 11 shows PIV vorticity fields for the hydrophilic acrylic sphere, and figure 12(*a*) shows the force coefficient for this PIV case. Figure 12(*a*) also shows the force coefficient for the backlit case from figure 3 (same data as figure 8*c*), showing very good agreement in the magnitude of C_F between the two cases, although the peak

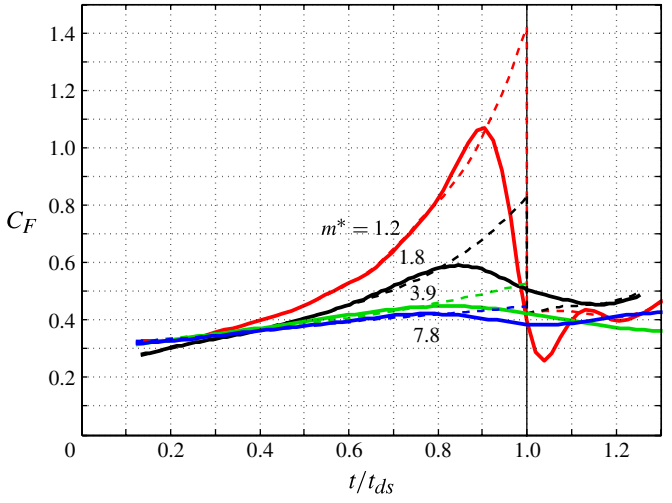

FIGURE 10. Force coefficients for each of the hydrophobic cases in figures 1 and 2 (solid lines), as well as composite force coefficients (dashed lines).

force coefficient occurs at slightly different times, emphasizing the sensitivity of C_F to the vortex shedding event.

In this study, we took PIV and position data, showing the growth and shedding of a vortex ring in the wake of the sphere. However, once the vortex ring is shed, the PIV data become difficult to interpret, since the vortex ring is obscured from view of the camera as it passes the sphere. In addition, vortex shedding occurs in three dimensions and may be out of plane. Therefore, multiple drops were required to gather data where the sphere and vortex ring remained in the laser plane during the entire time series.

A qualitative illustration of the ring-like vortex formation can be seen in figure 11. After impact the fluid is suddenly brought into motion, causing it to wrap up into a vortical structure as it passes towards the back of the sphere. On the right-hand side of the sphere, the circulation is counterclockwise, while the left-hand side is clockwise. As the sphere continues its descent, a small amount of circulation is left in the wake between $10.1 < t < 51.7$ ms. Two larger vortices continue to grow in strength until $t = 74.0$ ms, where the diameter of the vortex ring begins to grow outward. This outward growth is dominated by the negative vortex (left side) moving further to the left, while the positive vortex moves out of plane as it attempts to navigate its way past the sphere between $75.4 < t < 119.0$ ms. The circulation between the clockwise and counterclockwise circulation in figure 11 is conserved as expected for a vortex ring; this is discussed further in § 2. However, it should be noted that the counterclockwise vorticity begins to disappear as the sphere blocks the light from the laser at $t/t_{ds} = 1.34$–2.54.

As the vortex grows out and away from the sphere, the positive vortex motion on the sphere causes the sphere to move outward to the right in figure 11 ($t/t_{ds} = 1.34$–2.54). When the sphere is in the centre of the vortex ring, the flow field motion is downward. However, as the sphere moves to the right, the counterclockwise rotation begins to cause the sphere to move right and upward. Remarkably, this causes the sphere to slow even more and allows the vortex ring to pass by the

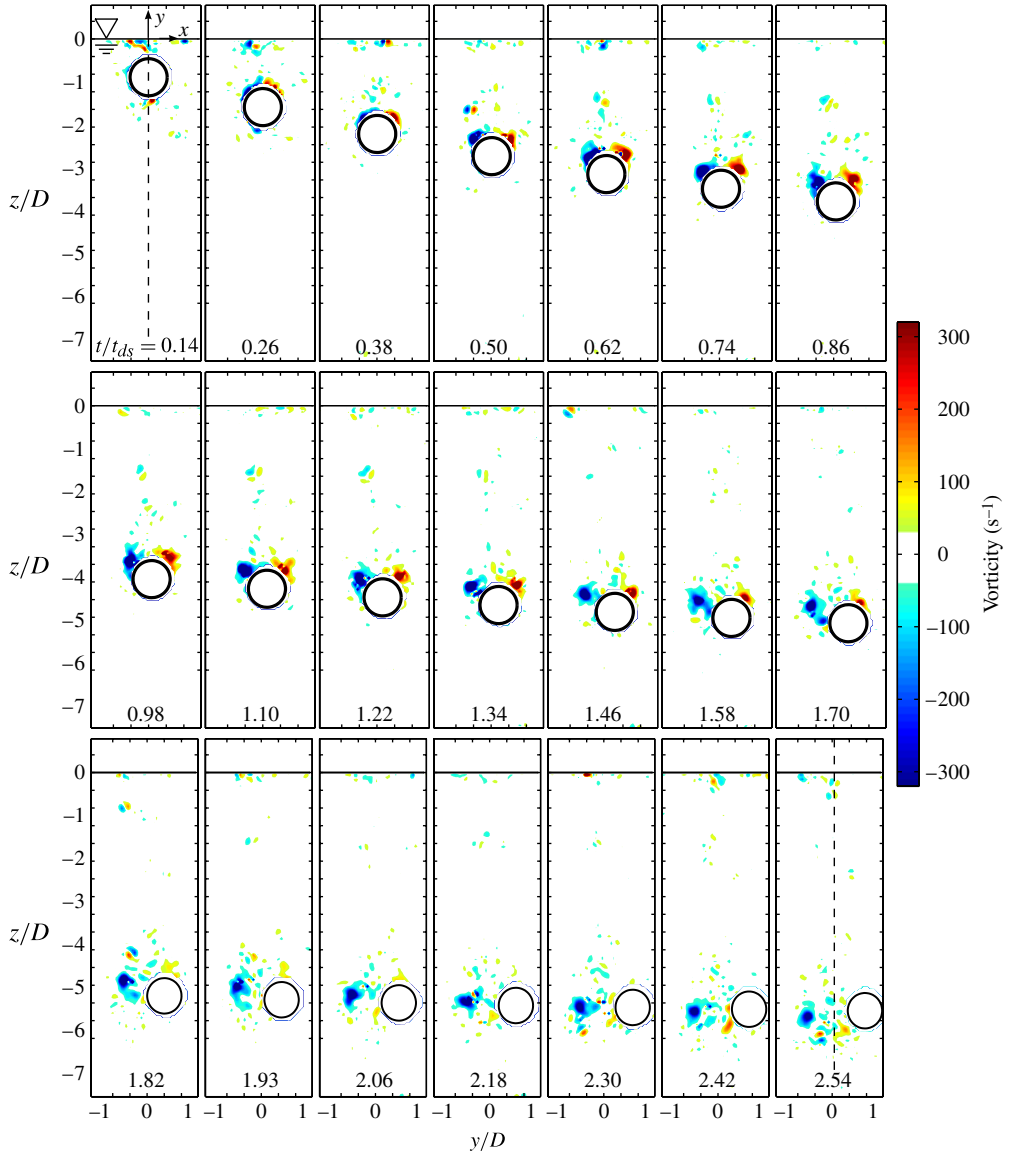

FIGURE 11. A time sequence of PIV vorticity contours for a hydrophilic (non-cavity-forming) acrylic sphere. This sphere has a diameter of $d = 25.4$ mm and an impact speed of 3.43 m s^{-1}, consistent with the acrylic case in figure 3 (although this is a different case).

sphere ($t/t_{ds} = 2.30$–2.54). Eventually, the vortex ring moves ahead of the sphere, and the positive vortex has some influence on the sphere, moving it back to the left and down (not shown). This motion moves the sphere somewhat back onto its previous path, as can be seen in the trajectory of the acrylic case shown in figure 5(*a*). The growth of the vortex ring beyond the diameter of the sphere indicates that it has now become detached from the sphere and that its circulation is no longer fed by the interaction of the sphere with the fluid.

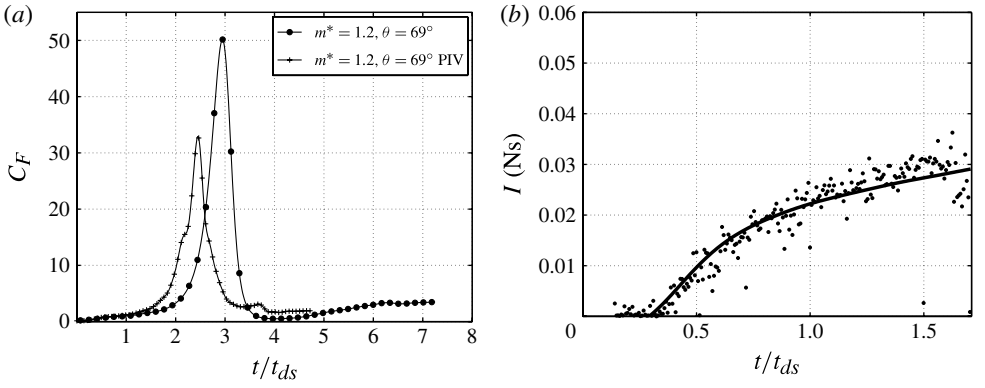

FIGURE 12. (*a*) Force coefficient (3.4) for the hydrophilic acrylic spheres presented in figures 3 and 11. The data for these two experiments compare well but the PIV case is slightly delayed, emphasizing their sensitivity to the vortex shedding event. (*b*) Impulse calculated from the PIV vorticity data (•, equation (4.1)), matches well with the theoretical prediction (−, equation (4.3)).

Using the circulation data, we can also determine the overall change in momentum of the fluid by determining the impulse of the vortex ring (Saffman 1995):

$$I(t) = \rho \Gamma \frac{\pi D_v^2}{4} \tag{4.1}$$

where Γ is the circulation (2.1) and D_v is the diameter of the ring. Figure 12(*b*) shows experimental impulse data computed using (4.1), which shows increasing impulse over time, as expected. The rate of change of vortex impulse gives rise to a hydrodynamic force, $\mathrm{d}I/\mathrm{d}t$.

4.2. *Force model*

In the non-cavity-forming cases, the hydrodynamic forces acting on the sphere can be modelled by the unsteady vortex shedding force discussed above, as well as added mass and buoyancy:

$$F = \frac{\mathrm{d}I}{\mathrm{d}t} - m_a \ddot{z} + F_B \ . \tag{4.2}$$

In these unsteady cases, the $\mathrm{d}I/\mathrm{d}t$ term accounts for the vortical wake generated by the sphere, so the classical drag term ($(1/2)\rho U^2 C_d \pi R^2$) is not used. Contrary to the cavity-forming cases, here the added mass and buoyancy terms can be directly computed. The added mass of the sphere is $m_a = (2/3)\pi R^3 \rho$ (Newman 1977), and buoyancy is constant ($F_B = (4/3)\pi R^3 \rho g$).

Since the total force F is known from (3.2), we should be able to use our experimental data to validate this model (4.2). However, the experimental impulse data shown in figure 12(*b*) are somewhat scattered, so $\mathrm{d}I/\mathrm{d}t$ cannot be precisely computed. Nevertheless, we can solve (4.2) for the impulse required to produce the motions observed in the experiments

$$I(t) = \int_{t_0}^{t} \left[F(t') + m_a \ddot{z}(t') - \tfrac{4}{3}\pi R^3 \rho g \right] \mathrm{d}t', \tag{4.3}$$

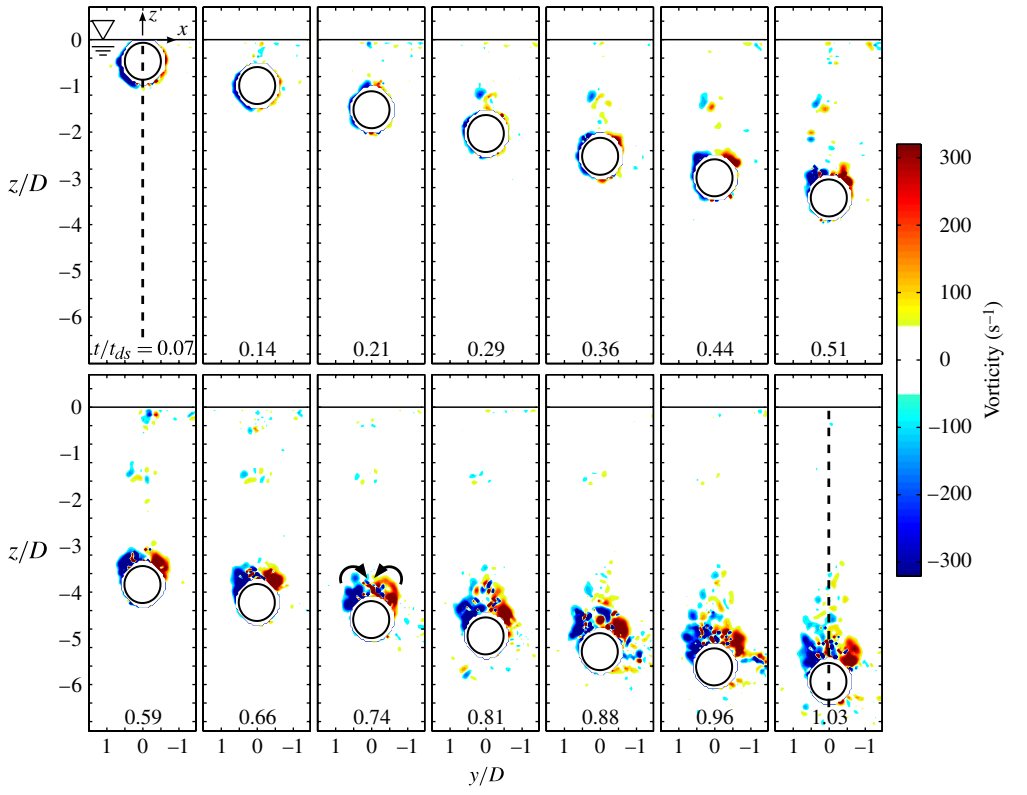

FIGURE 13. Time sequence of PIV vorticity contours for a hydrophilic (non-cavity-forming) ceramic sphere. This sphere has a diameter of $d = 25.4$ mm and an impact speed of 3.43 m s^{-1}, consistent with the ceramic case in figure 3 (although this is a different case).

where t_0 is the time at which the impulse begins accumulating in the vortex ring. Thus, experimental agreement in (4.3) would validate the force model (4.2). Figure 12(*b*) shows that (4.3) accurately determines the required impulse to balance the forces on the sphere, indicating that this model works well before the first vortex shedding event.

4.3. *Further model validation*

In figure 13, we present a second PIV case where a hydrophilic ceramic sphere ($m^* = 3.9$) is dropped from the same height as the acrylic sphere. Initially, circulation accumulates in the vortex ring similar to the acrylic case, since the two spheres have the same diameter and impact speed. At later times, however, the ceramic sphere maintains greater speeds than the acrylic, so more circulation is fed into the vortex ring. The vortex ring is never shed from the ceramic sphere while in the field of view, and the magnitude of its circulation continually increases as the sphere descends.

The force coefficient (3.4) and impulse (4.1) for the ceramic case are shown in figures 14(*a*) and 14(*b*), respectively. Figure 14(*b*) shows good agreement between the impulse (4.1) of the vortex ring in figure 13 and the present theory (4.3), once again demonstrating that this model accounts for the dynamics of these cases. The force coefficients in figure 14(*a*) for the present 'PIV case' (figure 13) show very good

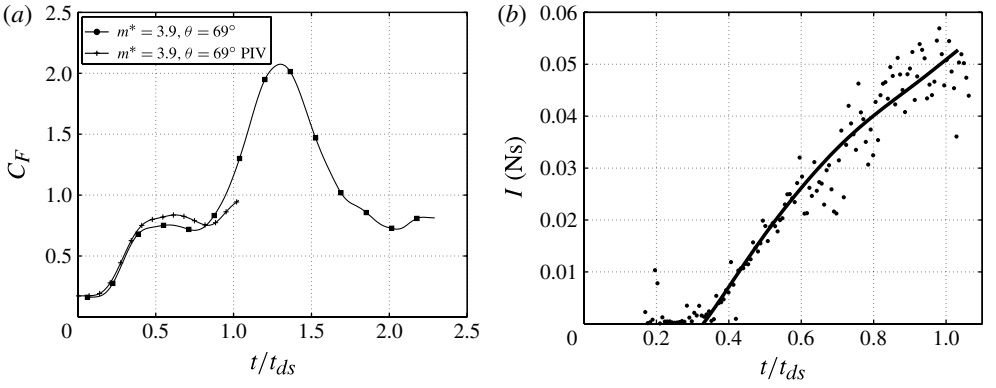

FIGURE 14. (*a*) Force coefficient (3.4) for the hydrophilic ceramic spheres presented in figures 3 and 13. (*b*) Impulse calculated from the PIV vorticity data (•, equation (4.1)), matches well with the theoretical prediction (−, equation (4.3)).

agreement with the backlit case (figure 3, same data as figure 8*d*), again demonstrating the accuracy and repeatability of the experimental methods.

5. Force model: cavity-forming cases

5.1. *PIV of cavity-forming cases*

The cavity-forming hydrophobic spheres also exhibit an unsteady hydrodynamic force coefficient. Once again, the acrylic sphere will be the subject of analysis in this section, since the acrylic sphere exhibits more unsteady behaviour than the higher-density-ratio ceramic and steel spheres. PIV results are presented to illustrate the flow field behaviour around the cavity. In this experiment, the fluid was imaged with a vertical light sheet emitted from a laser on the left side of the tank; no shadow appears to the right of the sphere because a mirror on the right side of the tank reflected the laser sheet back towards the sphere. The intense 'vorticity' at the pinch-off depth (at the pinch-off time) is actually an artifact of reflections of the laser sheet off the cavity surface as it collapses through the sheet, as shown in figure 15. Overall, the cavity-forming cases exhibit very little vorticity in general and no organized vortical structures in their wakes, as illustrated by the PIV vorticity fields in figure 15. These results agree with Bergmann *et al.* (2009) who also saw little vorticity in the presence of cavity formation. The vortical patches that are observed in figure 15 are insignificant, given their small size and relatively low vorticity levels. For the sake of argument, assume the small vortical patches in figure 15 are cross-sections of toroidal vortex rings. For such a vortex ring to be significant, its circulation would have to induce a downward vertical velocity on the order of the sphere impact speed $U_0 = 3.43$ m s^{-1}. The centreline velocity induced by a vortex ring is Γ/D_v, where the data in figure 15 show that $D_v \approx D = 25.4$ mm (i.e. the sphere diameter). The circulation is approximately $\Gamma \approx \bar{\omega} A_v$, where A_v is the area of the vortical patch and $\bar{\omega}$ is the average vorticity level. The maximum vorticity level observed in vortical patches that appear before pinch-off was approximately $\bar{\omega} \approx 150$ s^{-1}. Setting $\bar{\omega} A_v/D \sim U_0$ and noting that the cross-sectional area of the sphere is $A = \pi D^2/4$, the area of a vortical patch required to make it significant is $A_v/A = 4U_0/\pi D\bar{\omega} = 1.1$. Clearly, the area of the vortical patches observed in figure 15 is much smaller than $1.1A$, indicating that their effects are insignificant. By comparison, in the non-cavity-forming acrylic case

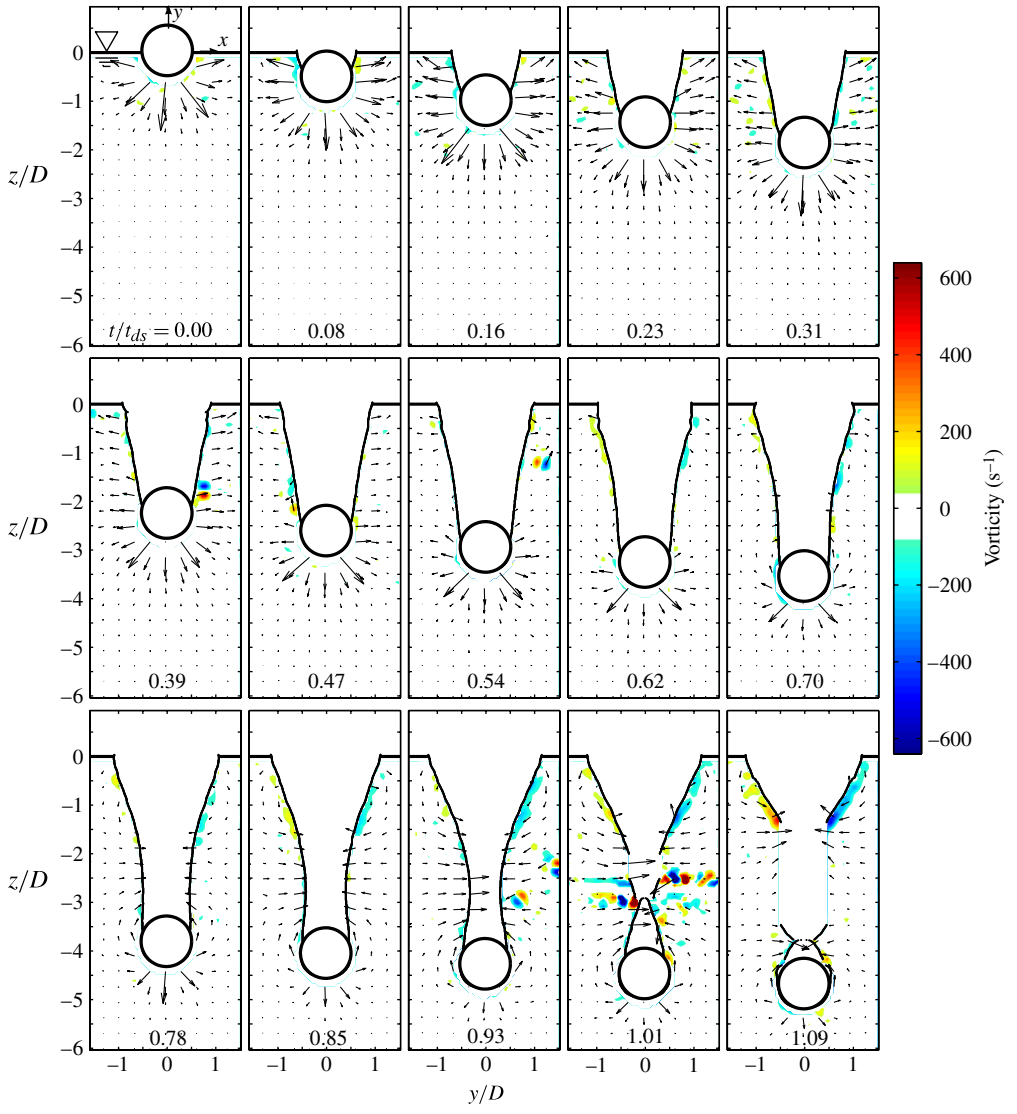

FIGURE 15. Time sequence of PIV velocity vectors and vorticity contours for a hydrophobic (cavity-forming) acrylic sphere. This sphere has a diameter of $d = 25.4$ mm and an impact speed of 3.43 m s^{-1}, consistent with the acrylic case in figure 1 (although this is a different case). The higher levels of vorticity at $t/t_{ds} = 1.01$ are due to the laser reflecting off the cavity wall during collapse.

of figure 11, the maximum vorticity level was approximately $\bar{\omega} \approx 300$ s^{-1}, making the required area of the vortical patches approximately $0.5A$, which is clearly observed in the later frames of figure 11.

Using (3.4), the hydrodynamic force coefficient is calculated and presented in figure 16. Figure 16 shows good agreement between the total force coefficient (obtained by spline fits to the measured position data via (3.4)) for the backlit trial (figure 1) and PIV trial (figure 15). Figure 16(*a*) illustrates how different the two lighting schemes are when viewed from the raw images; however, figure 16(*b*) shows

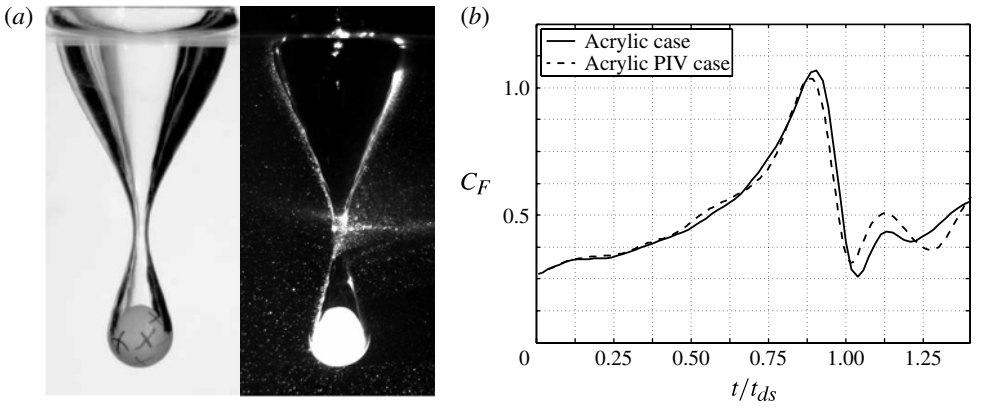

FIGURE 16. (*a*) Differences in lighting between backlit and PIV trials for the hydrophobic acrylic spheres presented in figures 1 and 15. (*b*) Force coefficients (3.4) show good agreement between the two cases, thus demonstrating the repeatability of the experimental and data processing methods.

how repeatable the data extraction method is for both types of lighting. This provides validation for the experimental methods for preparing and dropping the spheres and the numerical methods for interrogating the sphere position and fitting these data with a smoothing spline to derive the force coefficient. Figure 16 shows that the experimental methods used to obtain the 'experimental', smoothing-spline-derived force coefficient are highly accurate and repeatable.

5.2. *Potential flow cavity model*

A potential flow model is now developed for the cavity-forming cases. Scaling arguments show that viscous friction forces and surface tension forces are negligible in cavity-forming cases (see § 3.2). Further, PIV results show that the presence of a subsurface air cavity mitigates vortex shedding and effectively produces a potential-flow-like field (see § 5.1). Thus, the hydrodynamic forces on the sphere reduces to those from pressure forces

$$F = \int_S p(-\hat{\boldsymbol{n}} \cdot \hat{\boldsymbol{k}})\, \mathrm{d}S \tag{5.1}$$

where $\hat{\boldsymbol{k}}$ is the unit vector in the z-direction (positive upwards) and $\hat{\boldsymbol{n}}$ is the unit normal vector directed out of the sphere. In this section, a potential flow model is derived and used to compute the *unsteady*, *dynamic*, and *hydrostatic* pressure forces on the sphere during cavity-forming water-entry cases.

The potential flow cavity model described below follows that of Epps (2010). The method is an experimental-data-driven boundary-element method, with potential flow singularities placed near the fluid boundaries that are used to compute the flow field and, in particular, the pressure at the sphere surface. Epps (2010) employs three-dimensional axisymmetric potential flow singularities to model the sphere and cavity: the sphere is accounted for using a doublet, and the cavity is modelled as a source sheet formed by a point source (at the stagnation point) and several ring sources centred along the path of the sphere, as illustrated in figure 17. The strengths of the singularities are determined by enforcing the no-through-flow boundary condition

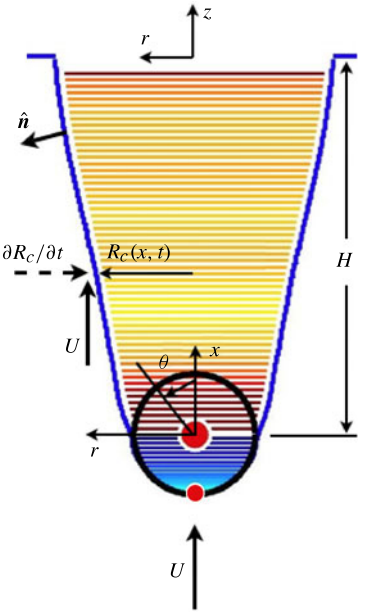

FIGURE 17. Illustration of the potential flow model, showing the sphere at depth H. In the sphere frame of reference, the free-stream velocity is U, and the cavity grows behind the sphere. Source rings are shaded according to their strength: red indicates positive (sources), and blue indicates negative (sinks). The large red dot at the centre of the sphere represents the dipole and the origin of the sphere reference frame. The smaller red dot at the bottom of the sphere represents the location of the point source.

at collocation points on the fluid boundaries (sphere surface and cavity surface). This model differs from a traditional boundary-element method in that the exterior boundaries (undisturbed free surface and tank walls) are ignored. The presence of the undisturbed free surface could easily be modelled by including image singularities above the surface. However, since the pressure induced by each such singularity scales by $(\text{distance})^{-4}$, these images would have virtually no effect on the forces predicted by the model once the sphere has descended any appreciable amount below the surface. The same argument holds for ignoring the tank walls.

The present model differs from other recently published numerical studies of cavity collapse (e.g. Eggers *et al.* 2007; Gordillo 2008; Gekle *et al.* 2009). These compute the flow field using three-dimensional point sources placed along the centreline of the cavity. In the present work, we observed the cavity shape experimentally and thus empirically determined the desired boundary conditions on both the cavity walls and sphere surface. In modelling these experiments, we first attempted to use this point-source model, but we found that no distribution of three-dimensional point sources existed that would satisfy our experimentally observed boundary conditions. In particular, we found that point sources placed along the trajectory centreline had too large a global effect and were unable to capture the rapid changes in boundary shape at the sphere surface and near the pinch-off location (i.e. in regions that violated the slender body assumption made in the above references). Therefore, the model we implemented employs three-dimensional ring sources with radii that track the local

cavity radius. These ring sources are able to capture the shape and evolution of the cavity surface, as observed in our experiments.

The present model requires the following experimental data as input: depth and speed of the sphere, $H(t) \equiv -z(t)$ and $U(t) \equiv -\dot{z}(t)$; and cavity geometry, $R_c(x, t)$, given from inspecting the cavity shapes in the raw images acquired during the experiment.

The model assumes that viscous forces and surface tension forces are negligible, and that the flow can be modelled as ideal, axisymmetric flow. Also, we assume that the pressure in the cavity is atmospheric, since the dynamic pressure required to draw air into the cavity is negligible (Gekle *et al.* 2010). Finally, consistent with our experimental observations we assume that the contact line is pinned to the equator of the sphere.

It is important to note that the potential flow model is three-dimensional, but since it is axisymmetric, we concern ourselves only with the meridional plane. To facilitate the algebra, two reference frames are used: the sphere frame (x, r), with origin at the centre of the sphere, and the lab frame (z, r), with origin fixed at the undisturbed free surface. It is assumed that the sphere did not deviate laterally during the impact event, so the radial direction is the same for both coordinate systems. Figure 17 shows that the axial directions are coincident $\hat{e}_x = \hat{e}_z$ and that the mapping between the coordinate systems is $x = z + H$.

The velocity potential is modelled using three-dimensional axisymmetric singularities located in the cavity (i.e. out of the fluid). As such, the total velocity potential is the sum of that from a doublet, a point source, and N ring sources:

$$\phi = \phi_d + \phi_p + \sum_{i=1}^{N} \phi_{s_i} \tag{5.2}$$

as illustrated in figure 17. The total fluid velocity in the meridional plane is

$$\boldsymbol{u} = u\,\hat{\boldsymbol{e}}_x + v\,\hat{\boldsymbol{e}}_r = \frac{\partial \phi}{\partial x}\,\hat{\boldsymbol{e}}_x + \frac{\partial \phi}{\partial r}\,\hat{\boldsymbol{e}}_r. \tag{5.3}$$

These equations are linear in the strength of the singularities. The strength of the doublet is set to $Q_d = UR^3/2$, as prescribed by the potential flow around a sphere in infinite fluid. The point source and N ring sources effectively form a *source sheet* that corrects for the presence of the subsurface air cavity. As such, the strength of the point source (Q_p) and N ring sources $(Q_{s_1}, Q_{s_2}, \ldots, Q_{s_N})$ are chosen to satisfy the no-through-flow boundary condition in the sphere frame of reference, which is

$$\boldsymbol{u}(x, r) \cdot \hat{\boldsymbol{n}}(x, r) = \begin{cases} U\cos(\pi - \theta) & \text{on sphere} \\ \dfrac{\dfrac{\partial R_c}{\partial t} + U\dfrac{\partial R_c}{\partial x}}{\sqrt{1 + \left(\dfrac{\partial R_c}{\partial x}\right)^2}} & \text{on cavity} \end{cases} \tag{5.4}$$

where $\hat{\boldsymbol{n}}(x, r)$ is the unit normal vector pointing out of the sphere/cavity. Equation (5.4) represents a linear system of equations that can be solved, and details of the numerical method are given in Appendix.

With the strengths of the singularities known for all time steps, the forces on the sphere are simply found by integrating the gauge pressure over the sphere surface,

where gauge pressure is computed by evaluating the unsteady Bernoulli's equation in the lab frame of reference

$$p - p_a = -\rho \frac{\partial \phi}{\partial t} - \frac{1}{2}\rho \left|\boldsymbol{u}\right|^2 - \rho g z \tag{5.5}$$

where the three terms are the unsteady, dynamic, and hydrostatic pressures.

The instantaneous force coefficient is found by integrating the gauge pressure (5.5) over the lower hemisphere and normalizing by the instantaneous dynamic pressure force $(1/2)\rho\left[U(t)\right]^2 \pi R^2$ in the usual way:

$$C_F = \frac{\displaystyle\int_0^{\pi/2} (p - p_a)\cos(\pi - \theta)\, 2\pi R^2 \sin(\pi - \theta)\, d(\pi - \theta)}{\frac{1}{2}\rho\left[U(t)\right]^2 \pi R^2}. \tag{5.6}$$

This yields force components

$$C_F = C_{F_{unsteady}} + C_{F_{dynamic}} + C_{F_{hydrostatic}} \tag{5.7}$$

which are defined positive when the force on the sphere is directed upwards (in the positive z-direction), causing a deceleration of the sphere.

Recently, Gekle *et al.* (2010) calculated that the gauge pressure in the cavity is nearly zero. Thus, there should be zero gauge pressure on the upper hemisphere of the sphere and at the sphere equator. However, since this model requires computing finite differences for $\partial R_c/\partial t$ and $\partial\phi/\partial t$, the resulting gauge pressure at the sphere equator is not necessarily zero, and the resulting unsteady force is incorrect. As a correction to the unsteady force, the average gauge pressure within 5° of the equator is computed, and this pressure coefficient is added to $C_{F_{unsteady}}$. The magnitude (typically less than 0.1) and variation of this correction can be seen in the fluctuations of the unsteady force coefficients shown in figure 19 below. This semi-empirical numerical model is now used to investigate the relative contributions of the unsteady, dynamic, and hydrostatic pressure forces.

5.3. *Cavity model results and comparison*

In order to illustrate some of the finer details of the cavity model, we return to the billiard ball case. Figure 18 shows a time series of images for the billiard ball impact case (same case as shown in figure 2), as well as the results of the potential flow simulation. Figure 19 shows the force coefficient results predicted by the numerical model, which compare well with the experimental (smoothing-spline-derived) C_F results from figure 8. The potential flow model correctly predicts the overall force coefficient for all cases, validating its applicability over a wide range of mass ratios.

Figure 19 also shows the unsteady, dynamic, and hydrostatic pressure forces on the sphere (solid red lines), as computed by the potential flow model. For comparison, consider the canonical theoretical problem of flow around a sphere in an infinite fluid (dashed orange lines). Upon integrating the gauge pressure on the leading half of the sphere, one finds the following theoretical force coefficients (Milne-Thomson 1968):

$$C_{F^{theoretical}_{unsteady}} = \frac{1}{2} - \frac{\frac{1}{2}\left(\rho\frac{2}{3}\pi R^3\, a(t)\right)}{\frac{1}{2}\rho\left[U(t)\right]^2 \pi R^2}, \tag{5.8}$$

$$C_{F^{theoretical}_{dynamic}} = -\frac{5}{8}, \tag{5.9}$$

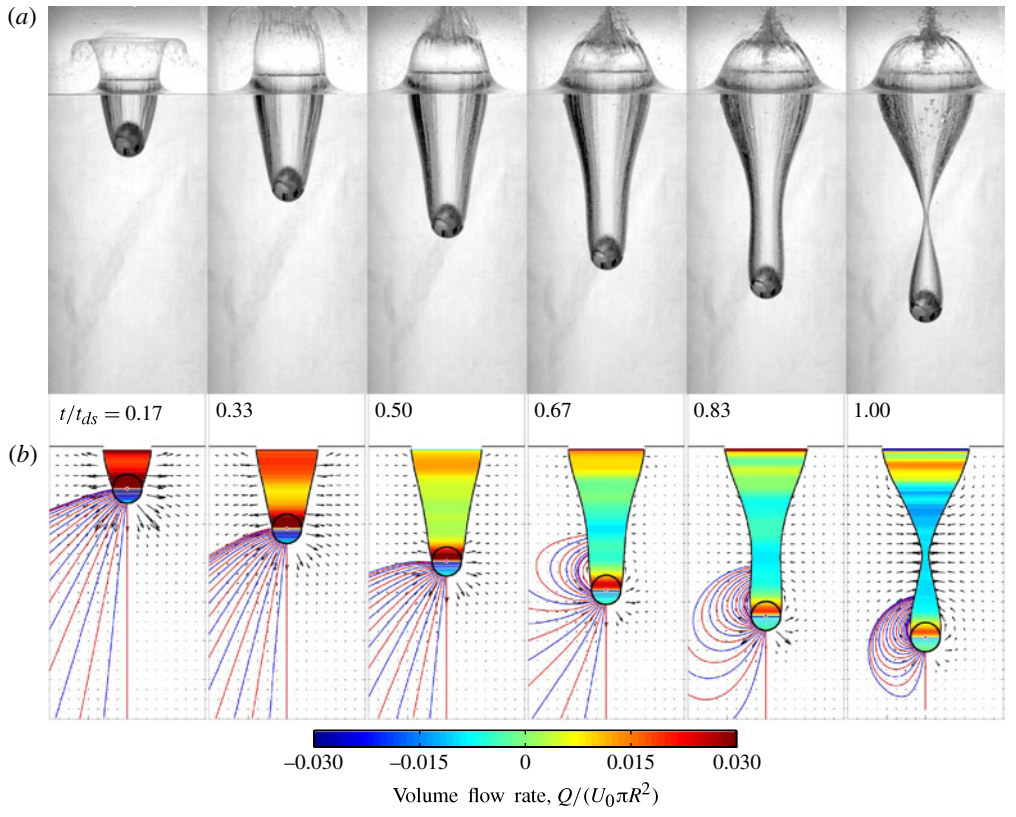

FIGURE 18. Film strip depicting water entry for the billiard ball case shown in figure 2 ($m^* = 1.8, D = 57.15$ mm, $U_0 = 5.67$ m s^{-1}). Cavity pinch-off (deep seal) occurs between the last frame shown here and the following frame. (*a*) Raw images from figure 2. (*b*) Potential flow simulation, including: sphere position and cavity shape, as interrogated from the raw images; velocity field, as computed by the potential flow model; instantaneous streamlines, plotted in alternating colours for clarity; and ring source strength, illustrated by the cavity shading at each depth. Images are synchronized in time.

$$C_{F^{theoretical}_{hydrostatic}} = \frac{\rho g H(t)\pi R^2}{\frac{1}{2}\rho\left[U(t)\right]^2\pi R^2} + \frac{\frac{1}{2}\left(\rho\frac{4}{3}\pi R^3 g\right)}{\frac{1}{2}\rho\left[U(t)\right]^2\pi R^2}. \tag{5.10}$$

The first term in the unsteady force equation accounts for the lab-fixed reference frame (which was used in the model), and the second term is the added mass of half a sphere (where a positive (i.e. upwards) sphere acceleration $a(t)$ causes a negative (i.e. downwards) force). The dynamic pressure force coefficient is a constant, since it depends only on geometry; for reference, the dynamic pressure force for a complete sphere is zero. The hydrostatic force is that given by the hydrostatic pressure acting at the equator and the buoyancy acting on a half-submerged sphere.

Let us compare the model results (solid red lines) and theoretical forces (dashed orange lines) shown in figure 19. The hydrostatic pressure force computed by the model matches almost exactly with the theoretical value (5.10), as expected by Archimedes' principle. This indicates that sufficient resolution was used in numerically integrating the forces in (5.6). There is also close agreement between the dynamic

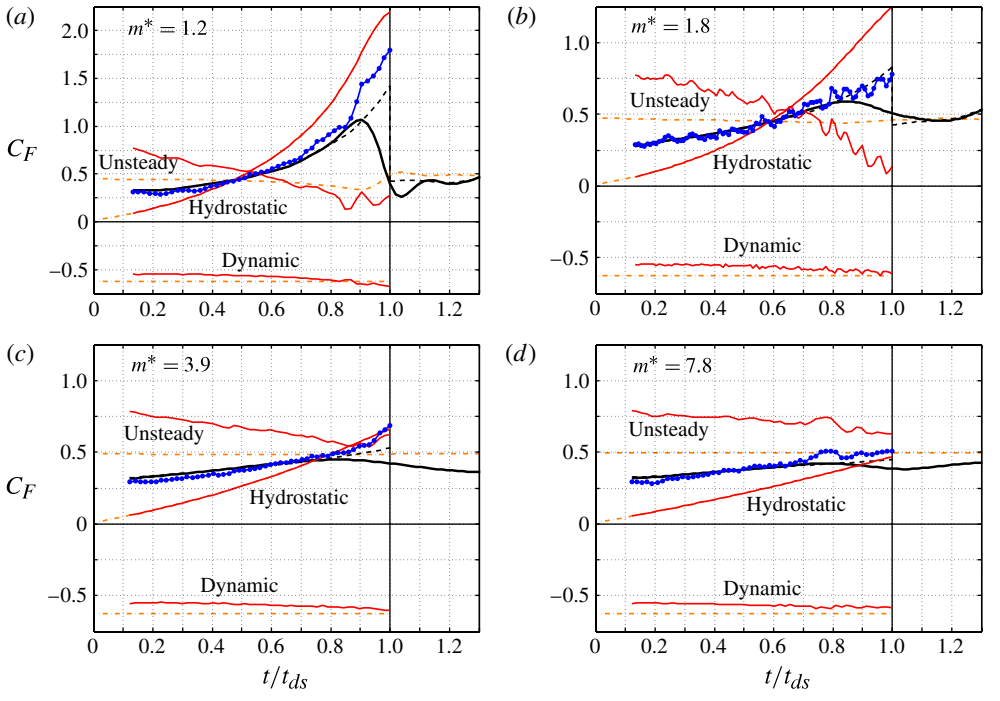

FIGURE 19. Force coefficient versus time normalized by pinch-off time for the cases in figures 1 and 18: force coefficient (3.4) (black line) derived from one spline fit to all the position data; composite force coefficient (3.4) (dashed black line) derived from one spline fit to the position data before pinch-off and another spline fit to the data after pinch-off; total force coefficient predicted by the potential flow model (5.7) (dotted blue line); unsteady, dynamic, and hydrostatic pressure forces predicted by the model (5.5) and (5.6) (red lines); theoretical unsteady, dynamic, and hydrostatic pressure forces (5.8)–(5.10) (orange dashed lines); (*a*) acrylic; (*b*) billiard; (*c*) ceramic; (*d*) steel.

pressure force computed by the model and that predicted by the theory (5.9). This indicates that the presence of the cavity does not dramatically alter the overall dynamic pressure force on the sphere. However, the unsteady pressure force on the sphere computed by the model is substantially different from the theoretical prediction (5.8). This indicates that the dominant effect of the cavity's shape and motion is to alter the unsteady pressure force on the sphere.

Since we prescribed the doublet strength based on the sphere velocity, which is consistent with the theoretical argument leading to (5.8), the unsteady pressure force due to the doublet alone should agree with this theoretical result. We have verified that these results agree within 1 % for all time steps, but these data are not shown in figure 19 since they would simply overlay the theoretical unsteady pressure force prediction. The effect of the single point source is negligible, so the cause of the difference between the total model unsteady pressure force and that predicted by the model is due to the ring sources representing the effect of the cavity.

To better understand the nature of the forces on the sphere computed by the potential flow model, consider figure 20. The potential flow simulation in figure 20 demonstrates how the unsteady pressure force changes much more dramatically for the low-mass-ratio acrylic sphere than it does for the high-mass-ratio steel sphere. The

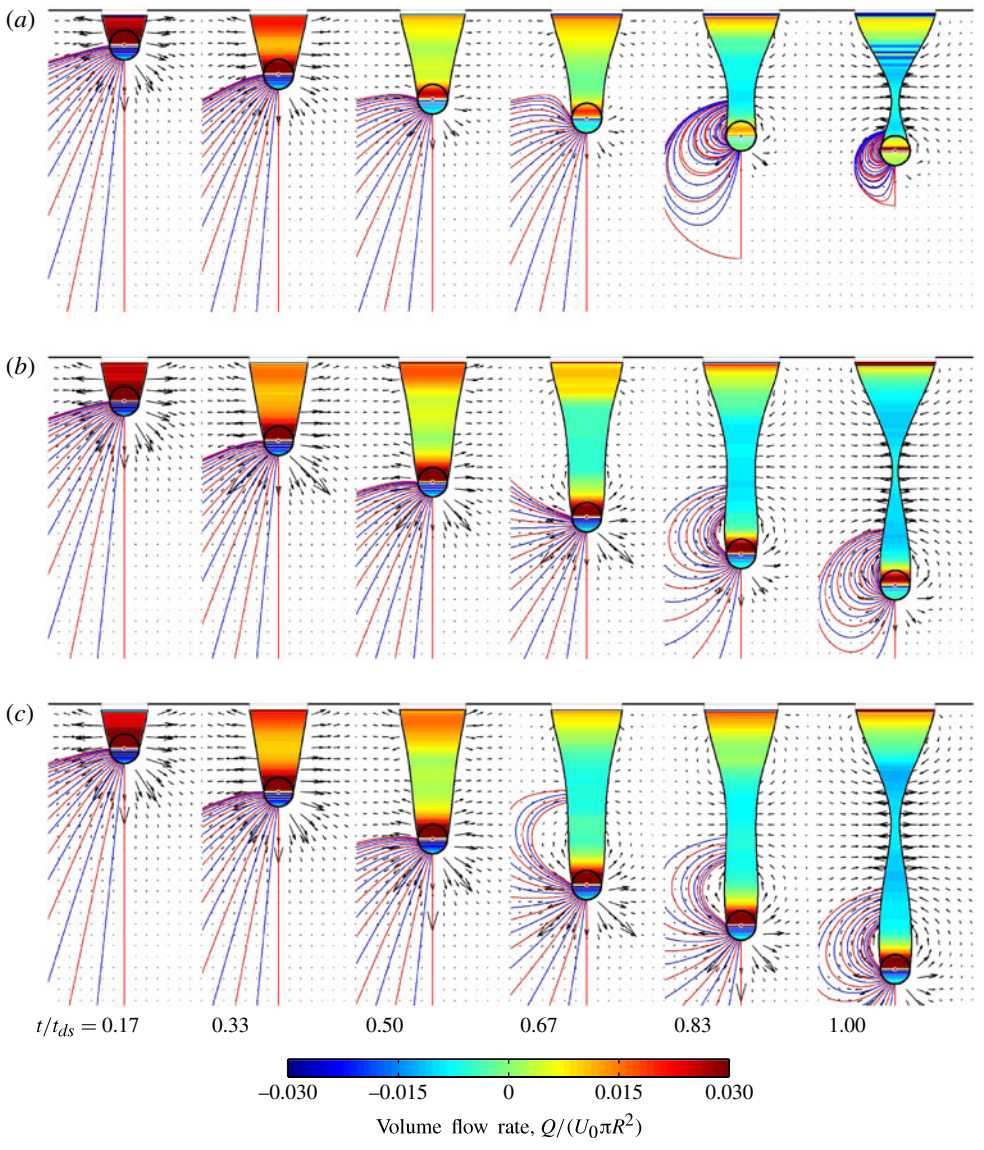

FIGURE 20. Potential flow simulation for the cases shown in figure 1: (*a*) acrylic: $m^* = 1.2$; (*b*) ceramic: $m^* = 3.9$; (*c*) steel: $m^* = 7.8$.

magnitude of the source strengths is coded in the colourmap, which is set consistent with the billiard ball case (figure 18). For the steel case, the magnitudes of the ring sources near the sphere are nearly constant from impact to pinch-off. In contrast for the acrylic case, the magnitudes of the ring sources near the sphere are large at impact but decay over the duration of the impact event and are near zero at the time of cavity pinch-off.

Figures 18–20 together show that the unsteady force is larger than the theoretical value for $t/t_{ds} \lesssim 0.75$, when a large portion of the rings in the cavity are positive-strength sources. This can be seen in the first few frames of figure 18, where most of

the rings in the cavity are shaded green to red. For later times, $0.75 \lesssim t/t_{ds} \leqslant 1$, the cavity collapses, many rings are negative-strength sources (i.e. sinks that draw fluid in) shaded green to blue in figure 18, and the unsteady force predicted by the model is less than that predicted theoretically.

The ring source strength is determined by the growth and collapse of the cavity. Neglecting the interaction between the rings, consider a slice of the cavity with radius $R_c(x, t)$ and axial length δx. The surface area of the slice is $S = 2\pi R_c \delta x \sqrt{1 + (\partial R_c/\partial x)^2}$, and the volume flow rate out of the slice required by (5.4) reduces to $Q_s = (\partial R_c/\partial t + U(\partial R_c/\partial x))2\pi R_c \delta x$. Thus, the strength of a ring will be positive (i.e. it will be a source) if the growth rate of the cavity $\partial R_c/\partial t$ and wall slope $\partial R_c/\partial x$ are positive. In these experiments, the rings behind the sphere equator all start as positive sources, pushing fluid outwards as the cavity grows. After some time, the cavity collapses for some period of time before the wall slope reaches vertical (i.e. $\partial R_c/\partial t < 0$ while $\partial R_c/\partial x > 0$ still). Eventually, the wall slope is sufficiently small for the ring to become a sink. As the cavity collapses further and the wall slope turns negative, the ring becomes an even stronger sink, drawing fluid into the cavity.

The results in figure 19 show that the unsteady pressure force on the sphere is modulated by the presence of the ring sources in the cavity, at some axial distance behind the sphere. It is vital that the formulation of the potential flow model utilizes three-dimensional potential flow constructs, thus enabling 'cross-talk' between each axial position along the cavity and the sphere surface. Prior works (e.g. Yan *et al.* 2009) have attempted to solve this problem using matched asymptotic analysis, representing the cavity strip-wise using two-dimensional sources (inner solution) and matching to a three-dimensional potential function describing the outer solution. Although their model may be sufficient to describe the cavity dynamics, it may lead to errors in representing the potential function on the sphere surface and computing the unsteady pressure force on the sphere. While many other models accurately capture cavity dynamics they rarely consider the forces on the spheres.

In general the instantaneous force coefficient is unsteady in time. The unsteady forces are of the order of the fluid inertial effects, making them quite significant for low-mass-ratio spheres. In the case of the higher-mass ratio-steel spheres, the force coefficients are nearly constant, which suggests that a simple second-order polynomial is sufficient to describe the sphere trajectory. However, the polynomial misses all of the unsteady dynamics present in the low-mass-ratio cases, suggesting that the piecewise spline fit to position is critical for analysing the forces. Data from the theoretical cavity model reveal similar trends, further illustrating the effects of mass ratio.

6. Conclusions

This paper presents a fully resolved examination of forces on spheres during water entry. The study shows that these forces are quite unsteady, especially for low-mass-ratio spheres (§ 3). The dynamics of non-cavity-forming hydrophilic spheres and cavity-forming hydrophobic spheres are unsteady for different reasons.

In the non-cavity-forming cases, the forces on the sphere are dominated by added mass, buoyancy, and the rate of change of impulse of a vortical wake (§ 4.1). PIV revealed that a ring-like vortical structure forms behind the sphere, carrying with it the impulse required to balance the change in momentum of the sphere. These PIV data also show that vortex shedding events correlate with peaks in the force coefficient.

Overall, the force coefficients are much larger in non-cavity-forming cases than in their cavity-forming counterparts.

In cavity-forming cases, the cavity acts to mitigate the formation of vortices, which allows cavity-forming spheres to maintain higher velocities after impact (§ 5.1). Here, the forces on the sphere are dominated by the hydrostatic, dynamic, and unsteady pressure components acting on the wetted portion of the sphere (i.e. the lower hemisphere). These forces can be approximated as the buoyancy and dynamic pressure acting on the leading hemisphere of a sphere, and an unsteady pressure that is modulated by cavity growth and collapse. As the cavity collapses, the inward and downward motion of the fluid above the sphere aids in decreasing the force coefficient in the moments before deep seal. Perhaps the most interesting finding is that the forces in the cavity-forming cases are considerably less than the unsteady forces in the non-cavity-forming cases which experience increased unsteady drag due to vortex shedding not seen in the cavity-forming case.

We present a model of the cavity as an axisymmetric source sheet (§ 5.2). Since the model employs three-dimensional (axisymmetric) singularities, the effect that the cavity has on the sphere surface is captured, and this model accurately describes the unsteady nature of the forces.

Acknowledgements

We gratefully acknowledge funding from the Office of Naval Research University Laboratory Initiative grant no. N00014-06-1-0445. We thank R. LaFoy, J. Gentils, A. Shih, A. Cantieny, L. Palmer, R. Munns, K. Bodily and J. Belden in helping with the acquisition, processing, and general support of this project. Discussions with J. Aristoff, J. Bush and G. McKinley were also very helpful.

Appendix. Potential flow simulation numerical method

This appendix provides details of the numerical methods used in the potential flow model discussed in § 5.2. The model employs a three-dimensional axisymmetric doublet, point source, and N ring sources, which are located in a coordinate system (x, r) that translates with the sphere, as shown in figure 17. Since the singularities are axisymmetric, we only concern ourselves with the meridional plane. The total velocity potential and fluid velocity in the meridional plane are given by (5.2) and (5.3), which are reproduced here:

$$\phi = \phi_d + \phi_p + \sum_{i=1}^{N} \phi_{s_i}, \tag{5.2}$$

$$\boldsymbol{u} = u\,\hat{\boldsymbol{e}}_x + v\,\hat{\boldsymbol{e}}_r = \frac{\partial \phi}{\partial x}\,\hat{\boldsymbol{e}}_x + \frac{\partial \phi}{\partial r}\,\hat{\boldsymbol{e}}_r. \tag{5.3}$$

The presence of the sphere is accounted for by a doublet located at $(0, 0)$. The potential function and fluid velocities at field point (x, r) induced by the doublet are

$$\phi_d(x, r) = Q_d \frac{x}{(x^2 + r^2)^{3/2}}, \tag{A 1}$$

$$u_d(x, r) = Q_d \frac{r^2 - 2x^2}{(x^2 + r^2)^{5/2}}, \tag{A 2}$$

$$v_d(x, r) = Q_d \frac{-3xr}{(x^2 + r^2)^{5/2}}, \tag{A 3}$$

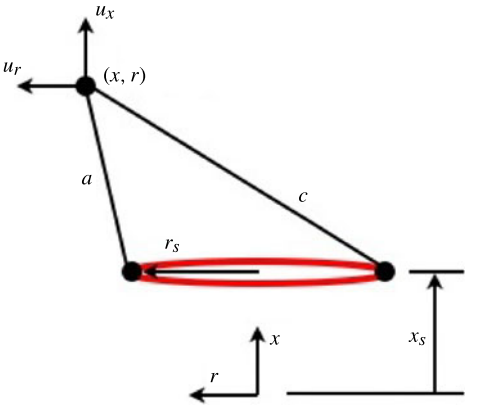

FIGURE 21. (Colour online) Illustration of a three-dimensional ring source.

where $Q_d = (1/2)UR^3$ is the strength of the doublet, as prescribed by the potential flow around a sphere of radius R moving at instantaneous speed $U \equiv U(t)$ in infinite fluid.

The point source and the N ring sources effectively form a source sheet that corrects for the presence of the subsurface air cavity. Each of these singularities enforces the no-through-flow boundary condition at a collocation point on the fluid boundary (e.g. the point source enforces no through-flow at the stagnation point $(-R, 0)$). The potential function and fluid velocities at field point (x, r) induced by a three-dimensional point source located at $(-x_p, 0)$ are

$$\phi_p(x, r) = Q_p \frac{-1}{4\pi \left((x + x_p)^2 + r^2\right)^{1/2}}, \tag{A 4}$$

$$u_p(x, r) = Q_p \frac{x + x_p}{4\pi \left((x + x_p)^2 + r^2\right)^{3/2}}, \tag{A 5}$$

$$v_p(x, r) = Q_p \frac{r}{4\pi \left((x + x_p)^2 + r^2\right)^{3/2}}, \tag{A 6}$$

where Q_p is the volume flow rate out of the point source and $x_p = R - R_{inset}$, where $R = 37.5$ px (pixels) is the sphere radius, and we choose $R_{inset} = 2$ px herein to avoid computing nearly infinite velocities at collocation points on the sphere surface near the point source. (For clarity, the cavity model is presented using the dimensional units of the images, length measured in pixels and time measured in frames elapsed, but the final force coefficients are properly non-dimensionalized.)

The potential function and fluid velocities at field point (x, r) induced by a three-dimensional ring source of strength Q_s, radius r_s, and axial position $x = x_s$ are derived as follows (see figure 21): since the volume flow rate out of the ring source is defined as Q_s, the potential function is derived by integrating the three-dimensional point sources of strength $Q_s/(2\pi r_s)$ distributed about the circumference of the ring

$$\phi_s(x, r) = \int_0^{2\pi} \frac{-[Q_s/(2\pi r_s)]}{4\pi \left((x - x_s)^2 + (r - r_s \cos\beta)^2 + (r_s \sin\beta)^2\right)^{1/2}} r_s \, \mathrm{d}\beta. \tag{A 7}$$

After much algebra, one obtains

$$\phi_s(x, r) = Q_s \frac{-K}{2\pi^2 a}, \tag{A 8}$$

$$u_s(x, r) = Q_s \frac{(x - x_s)E}{2\pi^2 c^2 a}, \tag{A 9}$$

$$v_s(x, r) = Q_s \frac{(r^2 - r_s^2 - (x - x_s)^2)E + c^2 K}{4\pi^2 r c^2 a}, \tag{A 10}$$

where

$$a = \sqrt{(x - x_s)^2 + (r - r_s)^2}, \tag{A 11}$$

$$c = \sqrt{(x - x_s)^2 + (r + r_s)^2}, \tag{A 12}$$

$$m = \frac{c^2 - a^2}{a^2}, \tag{A 13}$$

$$K = \bar{K}(-m) = \sqrt{m + 1}\ \bar{K}\left(\frac{m}{m + 1}\right), \tag{A 14}$$

$$E = \bar{E}(-m) = \sqrt{m + 1}\ \bar{E}\left(\frac{m}{m + 1}\right), \tag{A 15}$$

and $\bar{K}$ and $\bar{E}$ are complete elliptic integrals of the first and second kinds, respectively (Abramowitz & Stegun 1972).

The layout of the ring sources is as follows: for ring sources in the sphere,

$$r_s = (R - R_{inset}) \sin\theta, \tag{A 16}$$

$$x_s = (R - R_{inset}) \cos\theta, \tag{A 17}$$

where we choose $\theta = [91°, 96°, \ldots, 179°]$ (to achieve approximately the same spacing between these sources in the sphere as those in the cavity) and again $R_{inset} = 2$ px.

For ring sources in the cavity,

$$r_s = R_c(x_s, t) - R_{inset} \sqrt{1 + \left(\frac{\partial R_c(x_s, t)}{\partial x}\right)^2}, \tag{A 18}$$

$$x_s = [1, 2, \ldots, N_c]\delta x, \tag{A 19}$$

where we choose $\delta x = 1$ px (because it corresponded to the resolution of the cavity radius data $R_c(x_s, t)$ and so avoided interpolation of these data), and N_c is the number of sources in the cavity (which increases with cavity length).

The $R_c(x, t)$ data were determined using the high-speed images from each experiment. Raw cavity shape data were obtained using a Canny edge-detection algorithm to yield $\tilde{R}_c(x, t)$. These raw data for each time step were then fitted with a cubic smoothing spline to yield spatially smoothed cavity radius data, $\tilde{\tilde{R}}_c(x, t)$. Finally, an offset was added to the smoothed cavity radius data as a small correction that ensured that the cavity radius intersected the sphere equator ($R_c(x, t) = \tilde{\tilde{R}}_c(x, t) - \tilde{\tilde{R}}_c(0, t) + R$). This procedure yielded smoothed cavity shape data and ensured that the slope $\partial R_c/\partial x$ was smooth. However, the cavity radius data were not smoothed in time, so the temporal derivative $\partial R_c/\partial t$ still contains some noise.

The strengths of the point source and N ring sources are found by solving the no-through-flow boundary condition at the stagnation point $(-R, 0)$ and N additional collocation points (x_i, r_i), $i = 1, \ldots, N$, distributed over the sphere surface as follows:

$$(R\cos\theta_i, R\sin\theta_i) \quad \theta = [91^\circ, 96^\circ, \ldots, 179^\circ] \tag{A 20}$$

$$(x_{s_i}, R_c(x_{s_i}, t)) \quad x_s = [1, 2, \ldots, N_c]\delta x. \tag{A 21}$$

The boundary condition (which is most easily computed in the sphere frame of reference since the cavity radius data are tabulated as a function of distance behind the sphere) is given by (5.4), which is reproduced here:

$$\boldsymbol{u}(x, r)\cdot\hat{\boldsymbol{n}}(x, r) = \begin{cases} U\cos(\pi - \theta) & \text{on sphere} \\ \dfrac{\dfrac{\partial R_c}{\partial t} + U\dfrac{\partial R_c}{\partial x}}{\sqrt{1 + \left(\dfrac{\partial R_c}{\partial x}\right)^2}} & \text{on cavity} \end{cases} \tag{5.4}$$

where the unit normal vector pointing out of the sphere/cavity is

$$\hat{\boldsymbol{n}}(x, r) = \begin{cases} \cos\theta\,\hat{\boldsymbol{e}}_x + \sin\theta\,\hat{\boldsymbol{e}}_r & \text{on sphere} \\ \dfrac{-\dfrac{\partial R_c}{\partial x}\hat{\boldsymbol{e}}_x + \hat{\boldsymbol{e}}_r}{\sqrt{1 + \left(\dfrac{\partial R_c}{\partial x}\right)^2}} & \text{on cavity.} \end{cases} \tag{A 22}$$

Equation (5.4) can be written as a linear system of N equations in matrix form as

$$\boldsymbol{A}_s \cdot \boldsymbol{Q}_s = \boldsymbol{B}_0 - \boldsymbol{B}_d - \boldsymbol{b}_p Q_p \tag{A 23}$$

such that

$$\boldsymbol{B}_0 = \begin{cases} U\cos(\pi - \theta) & \text{on sphere} \\ \dfrac{\dfrac{\partial R_c}{\partial t} + U\dfrac{\partial R_c}{\partial x}}{\sqrt{1 + \left(\dfrac{\partial R_c}{\partial x}\right)^2}} & \text{on cavity} \end{cases} \tag{A 24}$$

$$\boldsymbol{B}_d = \boldsymbol{u}_d(x, r)\cdot\hat{\boldsymbol{n}}(x, r) \tag{A 25}$$

$$\boldsymbol{B}_p = \boldsymbol{u}_p(x, r)\cdot\hat{\boldsymbol{n}}(x, r) = \boldsymbol{b}_p Q_p \tag{A 26}$$

$$\boldsymbol{B}_s = \boldsymbol{u}_s(x, r)\cdot\hat{\boldsymbol{n}}(x, r) = \boldsymbol{A}_s \cdot \boldsymbol{Q}_s \tag{A 27}$$

where the through-flow velocity matrices $\boldsymbol{B}$ are all size $[N, 1]$, the point source influence matrix $\boldsymbol{b}_p$ is size $[N, 1]$, the point source strength Q_p is a scalar, the ring source influence matrix $\boldsymbol{A}_s$ is size $[N, N]$, and the ring source strength matrix is $\boldsymbol{Q}_s = [Q_{s_1}, \ldots, Q_{s_N}]^{\mathrm{T}}$. Given the experimental results, $\boldsymbol{B}_0$, $\boldsymbol{B}_d$, $\boldsymbol{b}_p$ and $\boldsymbol{A}_s$ are known, and the unknowns in (A 23) are Q_p and $\boldsymbol{Q}_s$.

For a given value of Q_p, (A 23) can, in theory, be solved for the ring source strengths, $\boldsymbol{Q}_s$. In practice, solving (A 23) by matrix inversion results in a non-physical set of source strengths that do not vary smoothly over the length of the cavity. This is due to the noise in computing $\partial R_c/\partial t$ from the experimentally measured cavity

shape data, $R_c(x,t)$. Although $R_c(x,t)$ was smoothed spatially (for each time step), it was not simultaneously smoothed temporally as well; therefore, the $\partial R_c/\partial t$ term in $\boldsymbol{B}_0$ contained measurement error, and this noise corrupted the direct matrix inversion method for finding $\boldsymbol{Q}_s$. Physically, the cavity shape varies smoothly in x, so source strengths should also vary smoothly in x as well. In order to solve for the source strengths, the following numerical method is used.

The numerical method is predicated on the fact that the total volume flow rate into the cavity in the absence of sources must be balanced by the total volume flow rate out of the source sheet. Since each ring source dominates the flow in its vicinity (by construction), the volume flow rate into each slice of the cavity is approximately balanced by the volume flow rate of the source at that station. Note that at this point, we do not know the point source strength. We proceed with an iterative procedure, whereby Q_p is estimated, $\boldsymbol{Q}_s$ is determined to satisfy (A 23), Q_p is updated, and so on until both Q_p and $\boldsymbol{Q}_s$ have converged.

The volume flow rate into a slice of the cavity is the through-flow velocity times the surface area. The surface area of each slice of the cavity between control points is

$$\boldsymbol{S} = \begin{cases} 2\pi R^2 \sin\theta\, \delta\theta & \text{on sphere} \\ 2\pi R_c \sqrt{1 + \left(\dfrac{\partial R_c}{\partial x}\right)^2}\, \delta x & \text{on cavity.} \end{cases} \tag{A 28}$$

For a given estimate of Q_p and $\boldsymbol{Q}_s$, the net inflow velocity and volume flow rate are

$$\boldsymbol{B}_{net} = \boldsymbol{B}_0 - \boldsymbol{B}_d - \boldsymbol{b}_p Q_p - \boldsymbol{A}_s \cdot \boldsymbol{Q}_s, \tag{A 29}$$

$$\boldsymbol{Q}_{net} = \boldsymbol{B}_{net} * \boldsymbol{S}, \tag{A 30}$$

where the '$*$' operator indicates element-wise vector multiplication, whereas '$\cdot$' indicates normal matrix multiplication. In order to obtain the next estimate for the source strengths, these net volume inflow rates are added to the ring source strengths

$$\boldsymbol{Q}_s^{next} = \boldsymbol{Q}_s^{current} + \boldsymbol{Q}_{net}. \tag{A 31}$$

Since each ring source strength dominates the velocity in its vicinity, iteratively updating $\boldsymbol{Q}_s$ using (A 29)–(A 31) converges to a set of smoothly varying $\boldsymbol{Q}_s$ that satisfy the no-through-flow condition (A 23), given the current estimate for Q_p.

Upon convergence of $\boldsymbol{Q}_s$, the point source strength, Q_p^{next}, is then set to cancel the velocity induced by the ring sources at the stagnation point $(-R, 0)$. This satisfies (5.4) at the stagnation point, because the doublet strength was already chosen to balance the free-stream velocity there. Evaluating (A 9) at $(x = -R, r = 0)$, noting that $\bar{E}(0) = \pi/2$ yields the velocity in the $\hat{\boldsymbol{e}}_x$ direction

$$u_s(-R,0) = \sum_{i=1}^{N} Q_{s_i} \frac{-(x_{s_i} + R)}{4\pi \left((x_{s_i} + R)^2 + r_{s_i}^2\right)^{3/2}}. \tag{A 32}$$

Thus, the next estimate for the point source strength is

$$Q_p^{next} = u_s(-R,0) 4\pi R_{inset}^2. \tag{A 33}$$

This iterative process continues for each estimate of Q_p by evaluating (A 29)–(A 31) until $\boldsymbol{Q}_s$ converges. Then Q_p is updated again by (A 32) and (A 33), and a new set of $\boldsymbol{Q}_s$ is found. This procedure continues until both Q_p and $\boldsymbol{Q}_s$ converge, which ensures that the no-through-flow boundary condition (5.4) is satisfied at all the control points and at the stagnation point.

With $(Q_d, Q_p, Q_{s_1}, Q_{s_2}, \ldots, Q_{s_N})$ known for all time steps, the gauge pressure at the sphere surface can be computed by evaluating the unsteady Bernoulli equation in the lab frame of reference,

$$p - p_a = -\rho \frac{\partial \phi}{\partial t} - \frac{1}{2}\rho \, |\boldsymbol{u}|^2 - \rho g z. \tag{A 34}$$

The partial derivative $\partial\phi/\partial t$ is computed in the lab frame of reference by a backward finite difference

$$\frac{\partial \phi}{\partial t} \approx \frac{\phi(R\cos\theta, R\sin\theta, t) - \phi(R\cos\theta - H(t) + H(t-\delta t), R\sin\theta, t - \delta t)}{\delta t}. \tag{A 35}$$

Note that a point $x(t)$ relative to the sphere centre at time t was located at $x(t-\delta t) = x(t) - [H(t) - H(t-\delta t)]$ in reference to the sphere centre at time $t - \delta t$, which leads to the above formulation. Numerical integration of the force coefficient (5.6) is performed over a fine mesh of surface points $(R\cos\theta_i, R\sin\theta_i)$, where we now set $\theta_i = [90°, 91°, \ldots, 180°]$.

REFERENCES

ABRAMOWITZ, M. & STEGUN, I. A. 1972 *Handbook of Mathematical Functions*. Dover.

ARISTOFF, J. M. & BUSH, J. W. M. 2009 Water entry of small hydrophobic spheres. *J. Fluid Mech.* **619**, 45–78.

ARISTOFF, J. M., TRUSCOTT, T. T., TECHET, A. H. & BUSH, J. W. M. 2010 The water entry of decelerating spheres. *Phys. Fluids* **22** (032102).

ASFAR, K. & MOORE, S. 1987 Rigid-body water impact at shallow angles of incidence. In *Proceedings of the Sixth International Offshore Mechanics and Arctic Engineering Symposium*, pp. 105–112. ASME, Virginia Polytechnic Inst. State Univ., Blacksburg, VA, USA.

BERGMANN, R., VAN DER MEER, D., GEKLE, S., VAN DER BOS, A. & LOHSE, D. 2009 Controlled impact of a disk on a water surface: cavity dynamics. *J. Fluid Mech.* **633**, 381–409.

BIRKHOFF, G. & ISAACS, R. 1951 Transient cavities in air–water entry. *Tech. Rep.* 1490. Navord Rep.

DE BOOR, C. 1978 *A Practical Guide to Splines*. Springer.

CLEVELAND, W. S. 1979 Robust locally weighted regression and smoothing scatterplots. *J. Am. Stat. Assoc.* **74** (367), 829–836.

DO-QUANG, M. & AMBERG, G. 2009 The splash of a solid sphere impacting on a liquid surface: numerical simulation of the influence of wetting. *Phys. Fluids* **21** (2), 022102.

DUCLAUX, V., CAILLÉ, F., DUEZ, C., YBERT, C., BOCQUET, L. & CLANET, C. 2007 Dynamics of transient cavities. *J. Fluid Mech.* **591**, 1–19.

DUEZ, C., YBERT, C., CLANET, C. & BOCQUET, L. 2007 Making a splash with water repellency. *Nat. Phys.* **3**, 180–183.

EGGERS, J., FONTELOS, M. A., LEPPINEN, D. & SNOEIJER, J. H. 2007 Theory of collapsing axisymmetric cavity. *Phys. Rev. Lett.* 094502.

EPPS, B. P. 2010 An impulse framework for hydrodynamic force analysis: fish propulsion, water entry of spheres, and marine propellers. PhD thesis, Massachusetts Institute of Technology, Cambridge, MA.

EPPS, B. P. & TECHET, A. H. 2007 Impulse generated during unsteady maneuvering of swimming fish. *Exp. Fluids* **43** (5), 691–700.

EPPS, B. P., TRUSCOTT, T. T. & TECHET, A. H. 2010 Evaluating derivatives of experimental data using smoothing splines. In *Proceedings of Mathematical Methods in Engineering International Symposium. MMEI, Lisbon Portugal*.

GAUDET, S. 1998 Numerical simulation of circular disks entering the free surface of a fluid. *Phys. Fluids* **10** (10), 2489–2499.

GEKLE, S., GORDILLO, J. M., VAN DER MEER, D. & LOHSE, D. 2009 High-speed jet formation after solid object impact. *Phys. Rev. Lett.* **102**, 034502.

GEKLE, S., PETERS, I. R., GORDILLO, J. M., MEER, D. & LOHSE, D. 2010 Supersonic air flow due to solid–liquid impact. *Phys. Rev. Lett.* **104**, 024501.

GHARIB, M., RAMBOD, E. & SHARIFF, K. 1998 A universal time scale for vortex ring formation. *J. Fluid Mech.* **360**, 121–140.

GILBARG, D. & ANDERSON, R. A. 1948 Influence of atmospheric pressure on the phenomena accompanying the entry of spheres into water. *J. Appl. Phys.* **19** (2), 127–139.

GLASHEEN, J. W. & MCMAHON, T. A. 1996 Vertical water entry of disks at low Froude numbers. *Phys. Fluids* **8** (8), 2078–2083.

GOLDMAN, D. I. & UMBANHOWAR, P. 2008 Scaling and dynamics of sphere and disk impact into granular media. *Phys. Rev.* E **77**, 021308.

GORDILLO, J. M. 2008 Axisymmetric bubble collapse in a quiescent liquid pool. I. Theory and numerical simulations. *Phys. Fluids* **20**, 112103.

GRUMSTRUP, T., KELLER, J. B. & BELMONTE, A. 2007 Cavity ripples observed during the impact of solid objects into liquids. *Phys. Rev. Lett.* **99**, 114502.

HOROWITZ, M. & WILLIAMSON, C. H. K. 2008 Critical mass and a new periodic four-ring vortex wake mode for freely rising and falling spheres. *Phys. Fluids* **20**, 101701.

VON KÁRMÁN, T. 1929 The impact on seaplane floats during landing. *Technical Notes* 321. National Advisory Committee for Aeronautics, Aerodynamic Institute of the Technical High School, Aachen, Washington, D.C., USA.

KOROBKIN, A. A. & PUKHNACHOV, V. V. 1988 Initial stage of water impact. *Annu. Rev. Fluid Mech.* **20**, 159–185.

LEE, M., LONGORIA, R. G. & WILSON, D. E. 1997 Cavity dynamics in high-speed water entry. *Phys. Fluids* **9**, 540–550.

MAY, A. & HOOVER, W. R. 1963 A study of the water-entry cavity. Unclassified NOLTR 63–264. United States Naval Ordinance Laboratory, White Oak, Maryland, USA.

MILNE-THOMSON, L. M. 1968 *Theoretical Hydrodynamics*, 5th edn. Dover.

MOGHISI, M. & SQUIRE, P. T. 1981 An experimental investigation of the initial force of impact on a sphere striking a liquid surface. *J. Fluid Mech.* **108** (1), 133–146.

NEWMAN, J. N. 1977 *Marine Hydrodynamics*. MIT.

RAFFEL, M., WILLERT, C., WILLERT, C. E. & KOMPENHANS, S. 1998 *Particle Image Velocimetry*. Springer.

SAFFMAN, P. 1995 *Vortex Dynamics*. Cabridge University Press.

TECHET, A. H. & TRUSCOTT, T. T. 2011 Water entry of spinning hydrophobic and hydrophilic spheres. *J. Fluids Struct.* **27** (5–6), 716–726.

THORODDSEN, S. T., ETOH, T. G., TAKEHARA, K. & TAKANO, Y. 2004 Impact jetting by a solid sphere. *J. Fluid Mech.* **499**, 139–148.

TRUSCOTT, T. T. 2009 Cavity dynamics of water entry for spheres and ballistic projectiles. PhD thesis, Massachusetts Institute of Technology, Cambridge, MA, USA.

TRUSCOTT, T. T. & TECHET, A. H. 2009*a* A spin on cavity formation during water entry of hydrophobic and hydrophilic spheres. *Phys. Fluids* **21**, 121703.

TRUSCOTT, T. T. & TECHET, A. H. 2009*b* Water entry of spinning spheres. *J. Fluid Mech.* **623**, 135–165.

WAGNER, H. 1932 Phenomena associated with impacts and sliding on liquid surfaces. *Z. Angew. Math. Mech.* **12**, 193–235.

WORTHINGTON, A. M. 1908 *A Study of Splashes*. Printed by William Brendon and Son, Ltd; reprinted by Macmillian Co., New York, 1963 edn. Longmans Green and Co., Plymouth..

YAN, H., LIU, Y., KOMINIARCZUK, J. & YUE, D. P. 2009 Cavity dynamics in water entry at low Froude numbers. *J. Fluid Mech.* **641**, 441–461.